Crystal ribcage: a platform for probing real-time lung function at cellular resolution in health and disease

Authors: Rohin Banerji[1]†, Gabrielle N. Grifno[1]†, Linzheng Shi[1], Dylan Smolen[1], Rob LeBourdais[1], Johnathan Muhvich[1], Cate Eberman[1], Bradley Hiller[2], Jisu Lee[2], Kathryn Regan[1], Siyi Zheng[1], Sue S. Zhang[1], John Jiang[1], Julia C. Breda[2], Riley Pihl[2], Katrina Traber[2], Sarah Mazilli[2], Giovanni Ligresti[2], Joseph P. Mizgerd[2], Bela Suki[1], Hadi T. Nia[1*]

Affiliations:
[1] Department of Biomedical Engineering, Boston University; Boston MA
[2] Pulmonary Center, Boston University School of Medicine; Boston MA
† These authors contributed equally to this work
[*] Corresponding author. Email: htnia@bu.edu

Abstract

Understanding the dynamic pathogenesis and treatment response in pulmonary diseases requires probing the lung at cellular resolution in real-time. Despite recent progress in intravital imaging, optical imaging of the lung during active respiration and circulation has remained challenging. Here, we introduce the crystal ribcage: a transparent ribcage that (i) allows truly multiscale optical imaging of the lung in health and disease from whole-organ to single cell, (ii) enables the modulation of lung biophysics and immunity through intravascular, intrapulmonary, intraparenchymal, and optogenetic interventions, and (iii) preserves the 3-D architecture, air-liquid interface, cellular diversity, and respiratory-circulatory functions of the lung. Utilizing these unprecedented capabilities on murine models of primary and metastatic lung tumors, respiratory infection, pulmonary fibrosis, emphysema, and acute lung injury we probed how disease progression remodels the respiratory-circulatory functions at the single alveolus and capillary levels. In cancer, we identified the earliest stage of tumorigenesis that compromises alveolar and capillary functions, a key state with consequences on tumor progression and treatment response. In pneumonia, we mapped mutual links between the recruited immune cells and the alveolar-capillary functions. We found that neutrophil migration is strongly and reversibly responsive to vascular pressure with implications for understanding of how lung physiology, altered by disease and anatomical location, affects immune cell activities. The crystal ribcage and its broad applications presented here will facilitate further studies of real-time remodeling of the alveoli and capillaries during pathogenesis of nearly any pulmonary disease, leading to the identification of new targets for treatment strategies.

Introduction

The lung is continuously exposed to mechanical, biological, and immunological stresses throughout its lifetime, and it is the site of many fatal pathologies such as primary and metastatic cancers, respiratory infections, and both obstructive and fibrotic diseases among many others. Exemplified by the COVID-19 pandemic, our understanding of lung pathophysiology is limited. Mechanistic understanding of the complex structure-function of the lung at the cellular level and

its remodeling at the earliest stages of disease requires characterization of cause-effect relationships at multiple scales down to cellular resolution.

Continuous mechanical motion and enclosure by the ribcage makes the lung one of the most challenging organs to study at cellular resolution in real-time while its key physiological functions are intact. Clinical imaging modalities (e.g., MRI, CT, and PET) lack the spatiotemporal resolution needed to resolve dynamic alveolar respiratory function, capillary flow, and cellular trafficking and motility. Histological analysis can visualize fixed lungs at subcellular resolution, however the temporal dynamics of lung microphysiology is entirely lost in these "snapshot" images. Recently, intravital microscopy has enabled high resolution imaging of microcirculation in real-time[1-5], which led to major discoveries in lung biology and immunity[2,5-7]. However, these methods compromise the respiratory function of the lung, a defining feature of the pulmonary system with crucial effects on the physics, biology, and immunity of the lung[8-11]. Furthermore, these approaches only visualize a few alveoli of the lung through a small imaging window, and cannot capture whole-organ heterogeneities (e.g., apex vs base lung mechanics) and have limited ability to track rare or dynamic events that may span beyond the imaging window.

Here, in a major departure from existing approaches, we introduce the crystal ribcage, a transparent ribcage that enables optical imaging of nearly the entire surface of a functioning murine lung. The crystal ribcage enables real-time probing of the lung at cellular resolution while its respiratory functions are preserved via positive- or negative-pressure ventilation (as in mechanically assisted or spontaneous breathing), while its circulatory functions are preserved through *ex vivo* pulmonary perfusion of whole blood or media of interest. The crystal ribcage combines the *in vivo* benefits, i.e., preserving the cellular diversity and complex architecture of the lung, with the benefits of organ-on-chip models, i.e., imaging capability and high controllability of microphysiology. These unique capabilities of the crystal ribcage in perturbing the biophysics and immunity of the lung through intrapulmonary, intravascular, and optogenetic interventions while visualizing real-time cellular events in a functioning lung provide enormous opportunities for understanding cause-effect relationships in the pathogenesis of pulmonary diseases.

To this end, we utilized the crystal ribcage to probe remodeling of alveolar and capillary functions in mouse models of primary and metastatic lung cancer, bacterial infection, pulmonary fibrosis, emphysema, and acute lung injury. We identified the earliest stage of tumorigenesis when alveolar structure-functions are compromised and probed the dynamic circulatory functions of capillaries remodeled by tumor growth and pneumonia. Utilizing the controllability of the crystal ribcage combined with the maintenance of *in vivo* complexity, we identified a dramatic and reversible mechano-responsiveness in immune cell migration.

Finally, the unique capabilities of crystal ribcage in imaging and controllability of a functioning lung are scalable to human whole-lung, and adaptable to other organs such as brain and liver. Given the recent advances in long-term maintenance of large animal and human lung[14,15], brain[16] and liver[17], our transformative approach opens new avenues in transplantation and organ regeneration research in addition to understanding the real-time cellular pathogenesis in functional organs.

Results

Development, validation, and capabilities of the crystal ribcage

The crystal ribcage is a transparent, biocompatible platform designed to provide a physiological environment for a functioning lung *ex vivo* and allows the first truly multiscale optical imaging of the lung in health and disease. The crystal ribcage allows 3-D imaging over the entire surface of the lung (**Fig. 1a**), while uniquely combining the benefits of *in vivo* mouse models (cellular diversity, 3-D lung architecture, breathing and circulation function) and *in vitro* organ-on-chip models[12] (imaging advantages and extensive, precise control over microphysiology) (**Fig. 1b**). We designed the crystal ribcage to mimic the geometry and key properties of the native ribcage to preserve the *in vivo* physiological conditions of the mouse lung during imaging. We used micro computed tomography (μCT) data of mouse chest cavities to create 3-D molds of the ribcage that were specific to the age and strain of mice of interest (in this study: C57/B6, FVB N/J and A/J strains, aged 6-18 weeks). This 3-D mold was used in multi-step additive, sacrificial and thermoforming processes to fabricate the crystal ribcage (**Fig. 1c**, **Extended Data Fig. 1**). To provide the same surface properties as the native parietal pleura in the mouse chest cavity, we engineered the internal surface of the crystal ribcage to be hydrophilic, so that the lung slides freely along it in its natural configuration during ventilation (**Extended Data Fig. 2, Extended Data Movie 1-4**). We fabricated the crystal ribcage to be 150 μm thick (similar to a glass coverslip) and confirmed that the ribcage's curved geometry did not cause optical aberrations (**Extended Data Fig. 3**). We fabricated two versions of crystal ribcage using polystyrene and polydimethylsiloxane (PDMS) as they are biocompatible, free of autofluorescence and ubiquitous in biological research. Polystyrene, used to fabricate petri-dishes, generates a rigid crystal ribcage that is easily scalable to large animal and human lungs, and allows ventilation of the lung using positive- or negative-pressure ventilation (as in mechanically assisted or spontaneous breathing). The rigid crystal ribcage closely mimics the *in vivo* ribcage in quiet breathing as the majority of the lung ventilation is performed by diaphragm[13] (**Extended Data Fig. 4**). PDMS generates a soft crystal ribcage that is partially deformable to mimic the macroscale ribcage deformation that occurs *in vivo* during exercise, sighs, and coughs. Additionally, the PDMS ribcage is pierceable and self-healing to enable intraparenchymal injections. Finally, we confirmed the crystal ribcage does not affect the alveolar respiratory function compared to the intact mouse ribcage (**Extended Data Fig. 5**).

To preserve the lung's circulatory and respiratory functions, the crystal ribcage is equipped with custom and commercial external ventilators (for both negative- and positive-pressure), pumps (uniform and pulsatile), sensors, data acquisition units and displays (**Fig. 1d**). Additionally, we fabricated a custom 6-degree-of-freedom arm for rotating the crystal ribcage (**Extended Data Fig. 6**), to image the entire lung surface using any optical lens objective. The ability to image the whole, functional lung surface in its native geometry (**Fig. 1e**) allows capturing the spatial heterogenies from the lung apex down to the base, which is necessary to probe key pulmonary diseases that present in specific locations, such as fibrosis (basal) and emphysema (apical). The ability to switch imaging magnification enables focusing and tracking of rare and potentially stochastic events at the cellular scale (**Fig. 1f**). We quantified respiratory function at this scale by tracking a specific region of interest over the entire normal inspiratory pressure range from 3 to 18 cmH_2O (**Fig. 1f**) by mapping the alveolar diameter (**Fig. 1g**) and sub-alveolar strain (normalized deformation) field (**Fig. 1h**). We probed remodeling of capillary function by imaging the vascular transport such as

cell trafficking and drug delivery, with high spatiotemporal resolution, in health and disease (**Fig. 1i**). Finally, we quantified the remodeling of the lung extracellular matrix (ECM) in cancer, and real-time migration of recruited or resident immune cells (**Fig. 1j**). We utilized these unprecedented capabilities to demonstrate that the crystal ribcage can be used to probe lung dysfunction in nearly any pulmonary disease or condition with parenchymal presentation, such as primary and metastatic breast cancer, pneumonia, emphysema (or chronic obstructive pulmonary disease), and fibrosis at the whole organ, whole lobe, and alveolar scales (**Fig. 1k, Extended Data Fig. 7**). We demonstrated that the disease presentation and remodeling of the alveolar structure-function differs dramatically in different diseases at the alveoli and capillary levels.

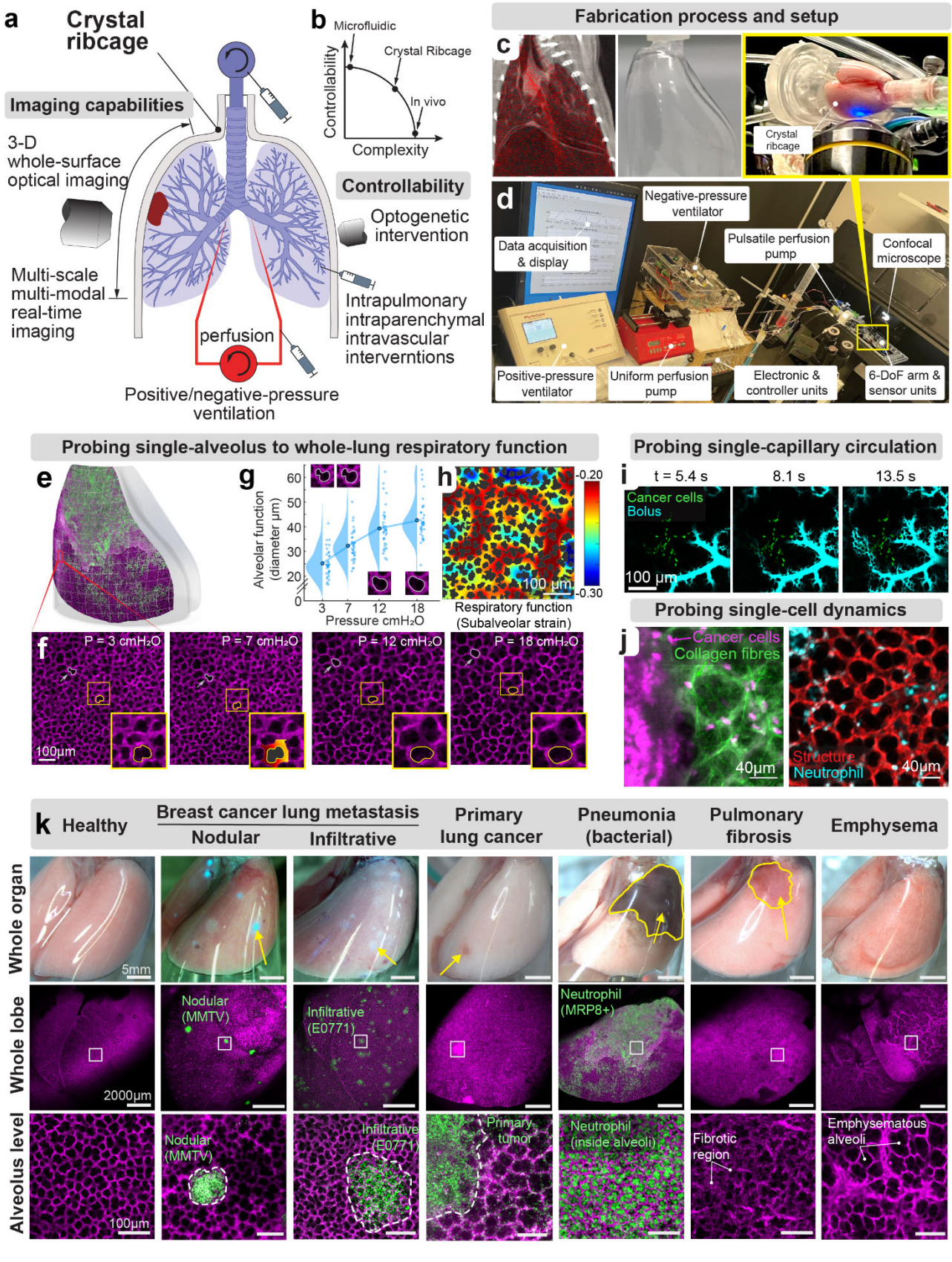
a
Crystal ribcage
Imaging capabilities
3-D whole-surface optical imaging
Multi-scale multi-modal real-time imaging
perfusion
Positive/negative-pressure ventilation
Controllability
Optogenetic intervention
Intrapulmonary intraparenchymal intravascular interverntions
b
Microfluidic
Crystal Ribcage
In vivo
Controllability
Complexity
Fabrication process and setup
c
Crystal ribcage
d
Negative-pressure ventilator
Data acquisition & display
Pulsatile perfusion pump
Confocal microscope
Positive-pressure ventilator
Uniform perfusion pump
Electronic & controller units
6-DoF arm & sensor units
Probing single-alveolus to whole-lung respiratory function
e
g
Alveolar function (diameter μm)
Pressure cmH₂O
h
100 μm
Respiratory function (Subalveolar strain)
f
P = 3 cmH₂O
P = 7 cmH₂O
P = 12 cmH₂O
P = 18 cmH₂O
100μm
Probing single-capillary circulation
i
t = 5.4 s
8.1 s
13.5 s
Cancer cells
Bolus
100 μm
Probing single-cell dynamics
j
Cancer cells
Collagen fibres
40μm
Structure
Neutrophil
40μm
k
Healthy
Breast cancer lung metastasis
Nodular
Infiltrative
Primary lung cancer
Pneumonia (bacterial)
Pulmonary fibrosis
Emphysema
Whole organ
5mm
Whole lobe
Nodular (MMTV)
Infiltrative (E0771)
Neutrophil (MRP8+)
2000μm
Alveolus level
Nodular (MMTV)
Infiltrative (E0771)
Primary tumor
Neutrophil (inside alveoli)
Fibrotic region
Emphysematous alveoli
100μm

FIGURE 1 | Development, capabilities, and application of crystal ribcage in pulmonary research. (a) Schematic representation of imaging, controllability, and intervention capabilities of the crystal ribcage for mechanistic studies of the lung in health and disease. **(b)** Crystal ribcage benefits from the imaging and controllability of organ-on-chip models while preserving the complexities and cellular diversity of in vivo models. **(c)** Age- and strain-specific μCT scans used to model the mouse chest cavity to fabricate crystal ribcage through a multistep additive and sacrificial fabrication process. **(d)** The portable platform to maintain, monitor, and record the physiological condition of the lung during imaging in the crystal ribcage. Crystal ribcage and a functioning lung is shown during real-time imaging. **(e)** Crystal ribcage allows the visualization of nearly the entire surface of the lung at the intact 3-D geometry. **(f)** The ability to navigate to desired regions of the lung, here two contoured alveoli, and image lung function at multiple spatial scales during the respiration cycle. **(g)** Analysis of lung function by measuring alveolar diameter as a function of air pressure and **(h)** map of the strain experienced by the alveolar septum. **(i)** Single capillary function in the crystal ribcage is assessed by real-time imaging of the capillary flow. **(j)** Single cell scale imaging allows probing relationships between cellular activity and alveolar-capillary structure-function. **(k)** Crystal ribcage is capable of probing nearly any pulmonary disease with parenchymal presentation, as demonstrated on models of breast cancer lung metastasis, primary lung cancer, respiratory infection, pulmonary fibrosis, and emphysema at length and functional scales starting at the whole organ down to single alveoli, single capillaries, and single cells.

Disruption of alveolar and capillary dynamics by tumor growth

Primary lung cancer is among the leading fatal cancers in both men and women[14]. The lung is also one of the major sites of metastasis for many cancer types including breast cancer[15]. While early steps of cancer cell extravasation and immune interactions have been studied using intravital microscopy in a lung immobilized by glue or vacuum[1,3], understanding of tumor dynamics during active respiration and circulation is lacking. Equipped with the crystal ribcage, we probed how tumor remodeling of the lung parenchyma disrupts respiratory and circulatory functions at the alveolus and capillary level. The ability to visualize the lung structure-function from single cell to whole-organ level (**Extended Data Fig. 8**, **Extended Data Movie 5**) has provided an unprecedented insight into lung-tumor interactions in mouse models of breast cancer lung metastasis and carcinogen-induced primary lung cancer.

To answer the long-standing questions surrounding remodeling of the structure and function of the alveoli by tumors, we investigated two mouse models of breast cancer lung metastasis with differential growth patterns. According to our previous work[16] and others'[17], tumor growth patterns are generally categorized as *nodular* (growth as a dense nodule that pushes the existing normal tissue outward) or *infiltrative* (cancer cells replace normal cells with minimal remodeling of surrounding architecture and blood vessels; also known as co-optive[18]), with distinct biological and clinical outcomes. Motivated by these works, we probed the differential alterations in structure and function in nodular vs infiltrative metastatic tumors modeled by murine breast cancer cell lines MCa-M3C-H2B-dendra2 and E0771-H2B-dendra2, respectively (**Fig. 2a, b**). We observed that alveoli filled with nodular tumors had impaired respiratory function, as they lacked the dynamic volume changes needed to participate in gas exchange during breathing. Interestingly, these alveoli remained maximally inflated across all alveolar pressures (**Fig. 2a**), indicating that the nodular cancer cells fill the entire airspace, distending the alveoli to their maximum volume. Additionally, this functional impairment extended up to 1-2 alveoli into the peritumoral region (**Extended Data Fig. 9**). In contrast, the infiltrative phenotype tumors did not compromise alveolar respiratory function either intratumorally or peritumorally, and the alveoli functioned similarly to regions far away from the tumor (**Fig. 2b**). Thus, infiltrative tumors merely take over the existing structure of the lung without drastically altering the alveolar structure-function relationship. In a carcinogen-induced model of primary lung cancer, early-stage tumors presented with a nodular-like

phenotype. However, the peritumoral alveoli presented as emphysematous, as multiple alveoli had coalesced into a single large alveolus (**Fig. 2c**). As a result, these emphysema-like alveoli were almost twice as large as alveoli far from the tumor and were not as responsive to increases in air pressure (**Fig. 2c**). This indicated that, despite not being directly filled with cancer cells, these alveoli still had reduced functionality compared to unaffected alveoli in the same lung.

Structural remodeling of the extracellular matrix (ECM) by tumors is known to be strongly correlated to progression and invasion of tumors[19,20]. To investigate whether lung structure is remodeled by breast cancer metastases, we investigated the collagen structure of nodular and infiltrative metastatic tumors using two-photon second-harmonic generation (SHG) microscopy. Analysis of the collagen structure showed that established nodules remodel the local extracellular matrix in the tumor region causing collagen fibers to become stretched (**Fig. 2d**), compared to the normally wavy collagen structures in the healthy lung. These straightened fibers indicate that the walls of the alveoli adjacent to nodular tumors are under tension (stretched) independent of the breathing cycle, such that alveoli cannot expand or contract, and thus cannot participate in gas exchange. In contrast, collagen fibers surrounding infiltrative tumor patches retained the same characteristic waviness seen in healthy tissue, implying that the structure-function of the alveoli remained unaffected in infiltrative tumor growth. We also assessed alveolar function by computing the strain in the walls of single alveoli using an image registration algorithm, which we adapted and validated for lung microscopy (**Extended Data Fig. 10-12**). Reduced strain in the septal walls during respiration indicates reduced alveolar functionality. In comparing the strain maps between the three different tumor types, the drastic structural remodeling by nodular metastatic breast cancer caused the most severe dysfunction in the surrounding alveoli, followed by the primary cancer nodules. Infiltrative cancer barely impacted local alveolar strain (**Fig. 2e**). In addition to impacting alveolar function, remodeling of lung collagen by nodular tumors has implications for long-term tumor progression, and has been linked to modulating immune behavior in the tumor microenvironment[21].

Next, we assessed the smallest nodule diameter that impacts single alveolus respiratory function. Analyzing the alveolar respiratory function in terms of tumor diameter, we found that nodules larger than 7-10 cells in diameter, approximately the size of one inflated alveolus, was the critical size needed to cause a reduction in the distensibility of local alveoli in nodular tumors (**Fig. 2f**). This can be attributed again to prevalent remodeling by the cancer bulk[22] which stretches the collagen fibers and in turn prevents alveolar septal walls from responding to changing air pressure. Interestingly, the interactions between cancer cells and alveoli are bi-directional: although single cancer cells do not impact alveolar distensibility, they instead experience deformation themselves during breathing. When arrested inside of capillaries, decreasing lung air pressure caused single cancer cells to experience substantial strain compared to cells in larger arterioles and venules (**Fig. 2g, Extended Data Fig. 13**). Experiencing higher (and cyclic) mechanical forces when located inside lung capillaries has long been studied as contributing to tumorigenesis in *in vitro* studies[23]; however, we, for first time to our knowledge, mapped the strains experienced by a single cancer cell in response to alveolar pressure in a functional lung with preserved complex 3-D architecture.

Given the dramatic remodeling of the alveolar respiratory functions by nodular tumors, we next asked how capillary function was affected. We studied the remodeled intra- and peritumor capillary structure-function in nodular cancer. The external controllable perfusion unit was used to deliver a bolus of fluorescent Cascade blue dextran (10 kDa) under steady 15 cmH_2O pressure-

controlled flow (approximate median vascular pressure at the mouse pulmonary artery[24]). The media perfused the entire lung inside the crystal ribcage. Time lapse imaging of the dye transport in the peri-tumor region revealed that the dye is excluded from the tumor bulk and peritumor up to ~100 μm (which is ~ two alveoli) away from the tumor, indicating that the native blood vessels near and inside the tumor lose circulatory function (**Fig. 2h**). The capillary remodeling not only reduced the intensity of the dye, but also delayed its arrival at the tumor in comparison to the surrounding healthy capillary bed far from the tumor (**Fig. 2i, j**). We observed such disruption of capillary function even in the presence of dispersed single cancer cells before the formation of established tumors (**Extended Data Fig. 14, Extended Data Movie 6**).

As convective flow through capillaries was insufficient to perfuse the tumor vasculature, we investigated the rate of passive diffusion in established nodular lung tumors. A smaller molecular weight fluorescent tracer (CBhydrazide, 550 Da), similar to small-molecule drugs, was perfused in a controlled manner until background fluorescence reached steady state. Continuous imaging of the tumors as small as 150 μm for over 60 minutes demonstrated a noticeable diffusion process into the tumor bulk (**Fig. 2j**). By fitting a mathematical model based on the diffusion equation to the rate of increase in fluorescence intensity inside the tumor (see Methods), we were able to estimate the diffusion coefficient of nodular tumors, a key parameter determining the rate of the drug and nutrient delivery to the core of the tumor, to be 3.25 μm s^{-1}, consistent with what is reported in melanoma tumors[25].

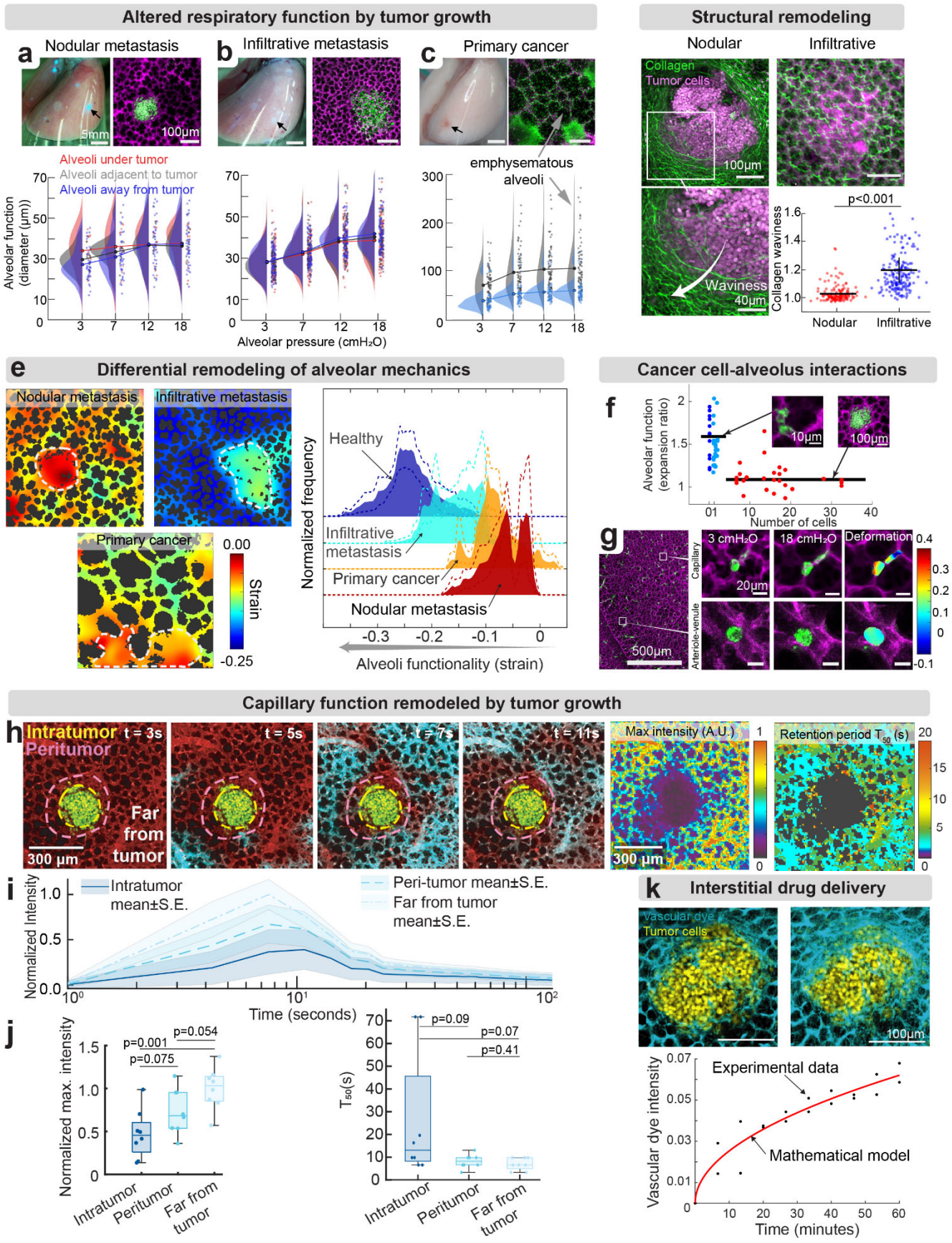
Altered respiratory function by tumor growth
a Nodular metastasis
b Infiltrative metastasis
c Primary cancer
5mm
100µm
Alveoli under tumor
Alveoli adjacent to tumor
Alveoli away from tumor
emphysematous alveoli
Alveolar function (diameter (µm))
Alveolar pressure (cmH₂O)
Structural remodeling
Nodular
Infiltrative
Collagen
Tumor cells
100µm
Waviness
40µm
p<0.001
Collagen waviness
Nodular
Infiltrative
e Differential remodeling of alveolar mechanics
Nodular metastasis
Infiltrative metastasis
Primary cancer
0.00
Strain
-0.25
Healthy
Infiltrative metastasis
Primary cancer
Nodular metastasis
Normalized frequency
Alveoli functionality (strain)
Cancer cell-alveolus interactions
f
Alveolar function (expansion ratio)
10µm
100µm
Number of cells
g
Capillary
Arteriole-venule
500µm
3 cmH₂O
18 cmH₂O
Deformation
20µm
Capillary function remodeled by tumor growth
h
Intratumor
Peritumor
Far from tumor
t = 3s
t = 5s
t = 7s
t = 11s
300 µm
Max intensity (A.U.)
Retention period T50 (s)
i
Intratumor mean±S.E.
Peri-tumor mean±S.E.
Far from tumor mean±S.E.
Normalized Intensity
Time (seconds)
j
Normalized max. intensity
p=0.001
p=0.054
p=0.075
Intratumor
Peritumor
Far from tumor
T50(s)
p=0.09
p=0.07
p=0.41
k Interstitial drug delivery
Vascular dye
Tumor cells
100µm
Experimental data
Mathematical model
Vascular dye intensity
Time (minutes)

FIGURE 2 | Multi-scale analysis of structure-function changes in different lung cancer models. Alveolar scale imaging of **(a)** nodular metastasis, **(b)** infiltrative metastasis, and **(c)** primary lung cancer used to quantify changes in alveolar diameter with changing pressure in intratumoral, peritumoral, and regions far from the tumor, **(d)** Surrounding structural changes were imaged using two-photon microscopy to quantify the collagen architecture by second harmonic generation imaging. **(e)** Altered alveolar functions compared in all three models by comparing the alveolar scale heatmap of strain between the lung at pressures of 12 and 7 cmH_2O. **(f)** Critical number of cells that alter the alveolar function. **(g)** Strain that arrested cancer cells experience during respiration cycle in capillaries vs arterioles/venules. **(h)** Real-time imaging of the circulatory function of the lung at the capillary level, and its alteration by nodular tumor. **(i)** The remodeled capillary function in the vicinity of nodular tumor was studied by quantifying the distribution and **(j)** retention of a vascular bolus delivered in the vicinity of a tumor nodule. **(k)** Passive diffusion of a fluorophore into the bulk of a nodular tumor is mapped, and the diffusion coefficient of the tumor was estimated by fitting a mathematical model.

Multiscale remodeling of respiratory and circulatory functions in pneumonia

Given the significance of pneumonia as one of leading global burdens of disease[26] even prior to COVID, we probed the impact of bacterial infection and acute injury on lung respiratory and circulatory functions at whole lobe down to single alveolus and single capillary scales. We used an established model of lobar bacterial pneumonia *S. pneumoniae* serotype 3 (Sp3) induced in MRP8-mTmG reporter mice in which MRP8+ cells (neutrophil dominant[27]) express green fluorescent protein (GFP) in the cell membrane. Imaging the whole lung through the crystal ribcage showed the hepatized (classic presentation of this disease) left apex, was densely packed with MRP8+ neutrophils at both the whole lobe and alveolar scales (**Fig. 3a**). The whole-organ respiratory function was compromised due to substantial edema and inflammation. However, the alveolus-level analysis of the respiratory function demonstrated substantial heterogeneities (**Fig. 3b**). Further analysis of the affected alveoli revealed that pneumonia-infected alveolar diameter remained small, indicating alveoli were collapsed rather than stretched due to both neutrophil recruitment and loss of vascular integrity resulting in pulmonary edema (**Fig. 3c**). Interestingly, while in both infection and cancer the affected alveoli were dysfunctional, the alveoli filled with cancer cells remain distended during the breathing cycle, and in contrast, the infected alveoli remained collapsed. Therefore, the mechanical forces that the alveolar and immune cells experience are dramatically different in the cancer vs infection. In comparison to disease-free alveoli, the inflammatory response to infection causes a decrease in strain (corresponding to reduced function) at the lobar and alveolar scales, and at the alveolar level, the strain was highly heterogeneous (**Fig. 3d**). This reduction in respiratory function is due partially to filling of the alveoli with incompressible liquid compared to healthy tissue (**Fig. 3e**), and as a result the compliance of the infected alveoli was even lower than the ones filled with nodular tumors (**Fig. 2e**).

Given the importance of systemic drug delivery, we next asked whether the recruitment of immune cells and edema in pneumonia affects the capillary function. We perfused a bolus of fluorescent tracer (CBhydrazide dye, 550 Da) through the pulmonary vasculature, and in real-time mapped the intravascular delivery of the perfusate in areas with partially collapsed alveoli. We found spatial heterogeneities of the fluorescent intensity (representative of a therapeutic drug; **Fig. 3f, Extended Data Movie 7**) in addition to heterogeneities in the arrival and clearance of the perfusate near the infected regions (**Fig. 3g-h**), representing the retention of the drug. Quantification of transport

dynamics surprisingly revealed that fluorescence intensity in the pneumonia-injured region was higher than in adjacent non-injured regions across all observed timepoints. Given the slower clearance of the dye, this indicates a compromised local vascular function in the injured alveoli which caused the dye to leak into the interstitium from where it cannot be easily cleared (**Fig. 3h**). Additionally, vascular dynamics were slower in the injured region in comparison to healthy tissue, suggesting that the dye was likely being transported by diffusion rather than convection in the injured tissue (**Fig 3f-i**). However, the leakiness of vessels in the case of pneumonia potentially allowed the perfused dye to be delivered the quickest (represented by time to reach its maximum intensity) as compared to the nodular tumor case (**Extended Data Fig. 15**).

Overall, we demonstrated the highly heterogeneous remodeling of alveoli and capillaries in pneumonia. This remodeling affects the respiratory and circulatory functions of the lung, which in turn affects (i) delivery of oxygen, nutrient, and therapeutics, and (ii) trafficking, recruitment, and clearance of immune cells with direct impact on the disease progression and treatment response. Using the crystal ribcage, we are now capable of studying the whole-lobe to single alveolus respiration-circulation dynamics to understand the real-time and alveolus-level dynamics of pneumonia pathogenesis and development and efficient delivery of novel therapeutics.

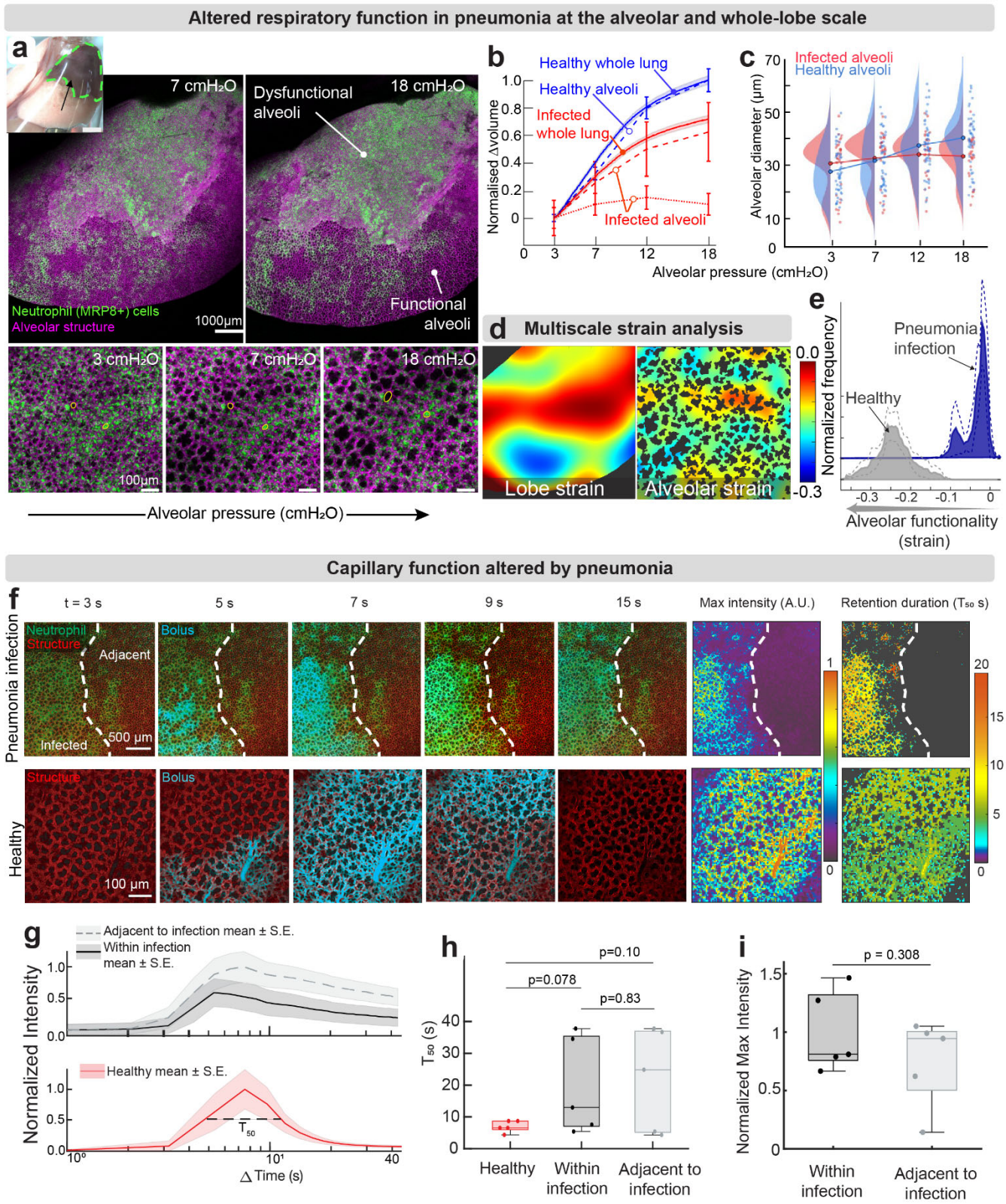
Altered respiratory function in pneumonia at the alveolar and whole-lobe scale
a
7 cmH₂O
18 cmH₂O
Dysfunctional alveoli
Functional alveoli
Neutrophil (MRP8+) cells
Alveolar structure
1000µm
3 cmH₂O
7 cmH₂O
18 cmH₂O
100µm
Alveolar pressure (cmH₂O)
b
Healthy whole lung
Healthy alveoli
Infected whole lung
Infected alveoli
Normalised Δvolume
Alveolar pressure (cmH₂O)
c
Infected alveoli
Healthy alveoli
Alveolar diameter (µm)
d
Multiscale strain analysis
Lobe strain
Alveolar strain
e
Pneumonia infection
Healthy
Normalized frequency
Alveolar functionality (strain)
Capillary function altered by pneumonia
f
t = 3 s
5 s
7 s
9 s
15 s
Max intensity (A.U.)
Retention duration (T₅₀ s)
Pneumonia infection
Neutrophil
Structure
Adjacent
Infected
500 µm
Bolus
Healthy
100 µm
g
Adjacent to infection mean ± S.E.
Within infection mean ± S.E.
Healthy mean ± S.E.
Normalized Intensity
Δ Time (s)
h
p=0.10
p=0.078
p=0.83
T₅₀ (s)
Healthy
Within infection
Adjacent to infection
i
p = 0.308
Normalized Max Intensity
Within infection
Adjacent to infection

FIGURE 3 | Impairment of alveolar respiratory and circulatory functions in pneumonia. (**a**) Entire left lobe imaged at 7 and 18 cmH_2O pulmonary pressure before navigating to smaller region of interest to study alveolar scale functionality. (**b**) Whole lung pressure-volume assessment of lung function does not account for heterogeneity in alveolar scale function. (**c**) Alveolar functionality assessed as diameter-pressure curves for infected and healthy alveoli. (**d**) Spatial maps of whole-lobe and alveolar scale strain show that lung tissue strain is reduced in areas filled with neutrophils recruited in pneumonia. (**e**) Strain reduction in alveoli filled with neutrophils show that alveolar function is severely impaired in pneumonia compared to healthy alveoli. (**f**) Capillary function in the pneumonia infected regions is compared against healthy lung by comparing the distribution and retention of fluorescently labelled perfusate. (**g**) Time course of fluorescence intensity in infected capillaries, capillaries adjacent to infection, and healthy capillaries in response to perfusion of a fluorescent bolus into the lung. (**h**) After perfusing a bolus into the lung, quantification of the time duration when fluorescence intensity in the capillary bed was greater than 50% of the maximum intensity, a metric of the tendency for dye to be retained in the capillary bed. (**i**) Maximum fluorescence intensity in healthy, infected, and infection-adjacent capillaries after delivery of a bolus.

Neutrophils are reversibly mechano-responsive to vascular pressure

While we observed that inflammation and recruitment of immune cells alter the alveolar and capillary functions, we endeavored to see if the relationship was mutual, i.e., whether the immune cell activity was also altered by changes in alveolar or capillary pressure. Intravital microscopy has previously visualized neutrophil migration in the lung through implanted windows on the mouse ribcage[28,29]. However, these approaches do not provide controllability of alveolar and capillary pressures. Using the crystal ribcage, we tracked single neutrophils as they migrate long distances in the lung in real-time while modulating (patho)physiologically relevant alveolar and vascular pressures and while we preserved the air-liquid interface to probe the effect of breathing and circulation dynamics on pulmonary immunity.

We observed dramatic and reversible changes in neutrophil migration speed in response to vascular pressure in mouse models of bacterial pneumonia and lipopolysaccharide (LPS) injury. In the lobar LPS model of acute injury in MRP8-mTmG mice[30,31] (**Fig. 4a, Extended Data Fig. 16**), we traced the paths of single neutrophils migrating within the injured alveoli in real-time (**Fig. 4b**) while increasing vascular pressure from 0 to 15 cmH_2O. We found that neutrophils migrated longer distances (**Fig. 4b**) and nearly twice as fast (**Fig. 4c**) over a five-minute period compared to zero vascular pressure. This change in speed was also reversible, as neutrophil speed responded to repeated step-changes in vascular pressure (**Extended Data Fig. 17, Extended Data Movie 8**). Importantly, we altered the vascular pressure while keeping the alveolar pressure of 7 cmH_2O constant to decouple the effects of respiration and passive circulation from neutrophil migration. Additionally, we maintained zero-flow conditions to decouple the effects of vascular flow and shear forces on immune cells[32]. We also measured the persistence (ratio of net cell displacement to total path length) of neutrophils while varying vascular pressure and found that it remained unaffected by changing pressure, implying that neutrophils migrate in random directions within the injury area, instead of moving with specific direction as would happen due to vascular flow during active circulation.

To confirm this surprising observation in an independent model, we induced bacterial pneumonia (Sp3) in the left lobe of MRP8-mTmG mice to model infection and found that neutrophils recruited into the capillaries, interstitium and alveolar air space. Imaging infected alveoli (**Fig. 4e**) and tracing migration path lengths (**Fig. 4f**) revealed that neutrophils located in the vascular and interstitial space also migrated a great deal compared to intra-alveolar neutrophils. The neutrophils

in the vasculature and interstitium moved almost twice as fast when vascular pressure was increased to 15 cmH_2O similar to LPS-induced injury, while neutrophils located in the intra-alveolar space maintained their low speed of migration regardless of vascular pressure changes (**Fig. 4g**). The persistence of neutrophils in the pneumonia model was also independent of changes in vascular pressure. We concurrently found that neutrophil speed did not change in response to alveolar pressure (**Fig. 4i**). Lastly, we observed that neutrophils dramatically changed shape and speed while migrating in the lung capillaries. We found that migration speed was directly correlated to cell aspect ratio and inversely related to circularity (**Fig. 4j, Extended Data Movie 9**) implying that they become more elliptical when moving faster.

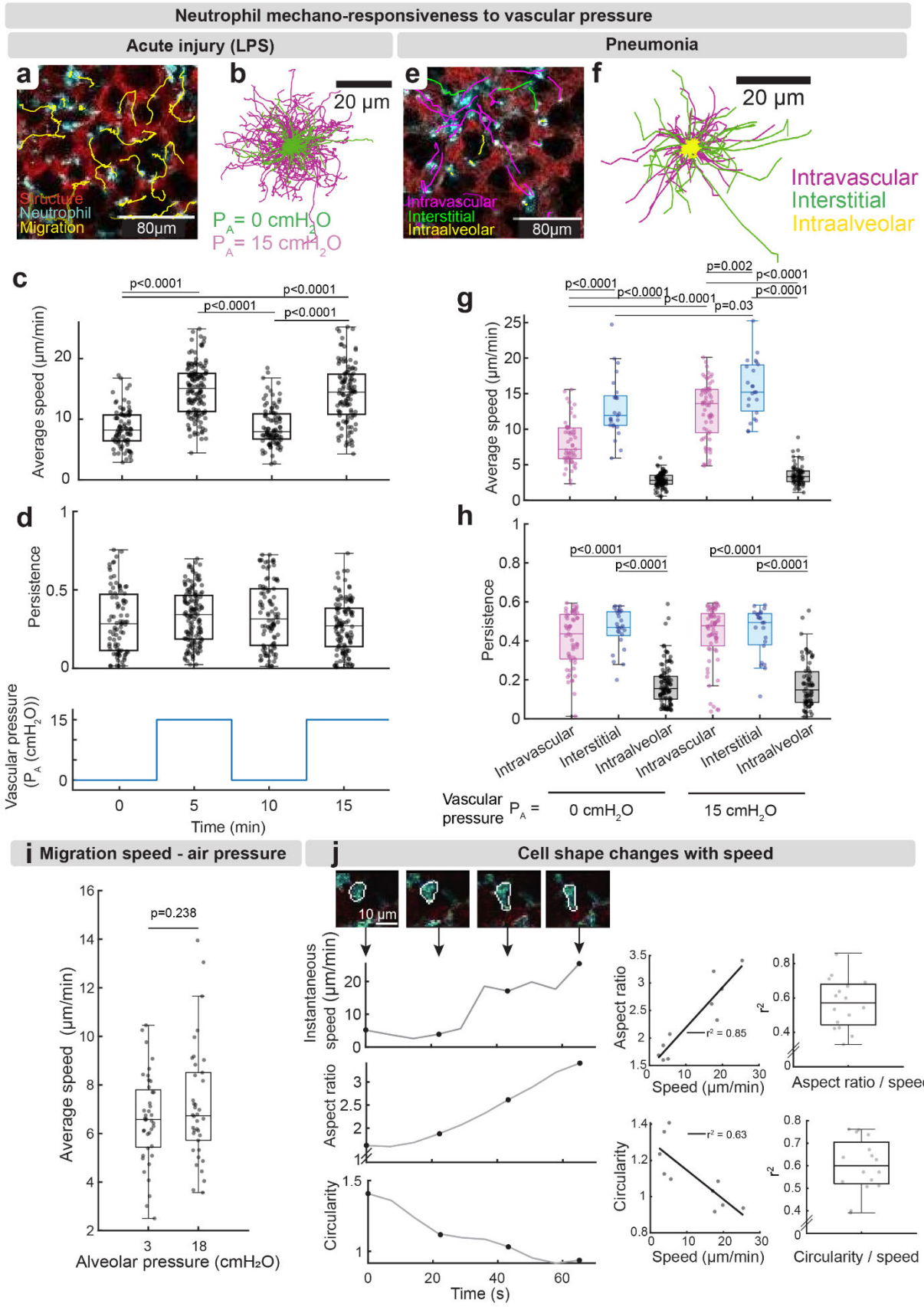
Neutrophil mechano-responsiveness to vascular pressure
Acute injury (LPS)
Pneumonia
a
Structure
Neutrophil
Migration
80µm
b
20 µm
P_A = 0 cmH2O
P_A = 15 cmH2O
e
Intravascular
Interstitial
Intraalveolar
80µm
f
20 µm
Intravascular
Interstitial
Intraalveolar
c
Average speed (µm/min)
p<0.0001
p<0.0001
p<0.0001
p<0.0001
g
Average speed (µm/min)
p<0.0001
p<0.0001
p<0.0001
p=0.03
p=0.002
p<0.0001
p<0.0001
d
Persistence
Vascular pressure (P_A (cmH2O))
Time (min)
h
Persistence
p<0.0001
p<0.0001
p<0.0001
p<0.0001
Intravascular
Interstitial
Intraalveolar
Intravascular
Interstitial
Intraalveolar
Vascular pressure P_A =
0 cmH2O
15 cmH2O
i Migration speed - air pressure
Average speed (µm/min)
p=0.238
Alveolar pressure (cmH2O)
j Cell shape changes with speed
10 µm
Instantaneous speed (µm/min)
Aspect ratio
Circularity
Time (s)
Aspect ratio
r² = 0.85
Speed (µm/min)
r²
Aspect ratio / speed
Circularity
r² = 0.63
Speed (µm/min)
r²
Circularity / speed

FIGURE 4 | Neutrophil migration is reversibly mechano-responsive to vascular pressure. (**a**) Representative image of neutrophil migration with cell trajectories (magenta) in the LPS model of acute lung injury. (**b**) Neutrophil migration map of paths travelled by single neutrophils over a 5-minute imaging interval. (**c**) Neutrophil average speed increases with vascular pressure and is reversible in LPS-damaged lungs (n = 3 mice). (**d**) Persistence directionality of neutrophil migration in LPS-damaged lungs. (**e**) Representative traced neutrophil migration in intra-alveolar (yellow), interstitial (cyan), and intravascular (magenta) spaces in Sp3 pneumonia lungs at a pulmonary artery pressure (PA) of 15 cmH_2O. (**f**) Neutrophil migration map for 15 cmH_2O hydrostatic perfusion pressures in pneumonia lungs for 5 minutes. (**g**) Neutrophil average speed and (**h**) persistence in intra-alveolar, interstitial, and intravascular spaces under 0 or 15 cmH_2O hydrostatic perfusion pressures in pneumonia lungs (n = 3 mice). (**i**) Neutrophil average speed in pneumonia lungs under alveolar pressures (P_{alv}) of 3 versus 18 cmH_2O (n = 2 mice). (**j**) Representative changes in single neutrophil speed, aspect ratio, circularity of the same neutrophil with its respective aspect ratio vs. speed and circularity vs. speed regressions, and the regression coefficient of determination of aspect ratio vs. speed and circularity vs. speed of a population of neutrophils (n = 27 cells pooled across n = 3 mice). Box charts indicate median, upper and lower quartiles, and maximum and minimum values that are not outliers of the scattered datapoints.

Respiration-circulation coupling is disrupted in lung injury

Lung respiration and circulation dynamics are strongly coupled. Assessments of respiration-circulation function at the whole organ level have shown that there is a delicate coupling between the two that regulates the diameter of large blood vessels, which in turn determines pulmonary vascular resistance[33]. However, to our knowledge respiration-circulation coupling has not been characterized at the alveolar-capillary level in real-time. The crystal ribcage enables both imaging and tracking of single capillaries during precisely controlled physiological ventilation and circulation conditions to probe the coupling between these two functions of the lung in health and disease. Taking advantage of these unique capabilities, we quantified the effect of respiration-circulation coupling on the distension of capillaries and arterioles/venules in healthy lungs by simultaneously varying alveolar and vascular pressure across a range of physiologically relevant pressures (**Fig. 5a**, **Extended Data Fig. 18**). We found in arterioles-venules that increasing air pressure over the entire normal inspiratory pressure range from 3 cmH_2O to 18 cmH_2O caused vascular diameter to first increase and then decrease, creating a "bell shaped" curve, for all vascular pressures. This interesting pressure response implies that there is an optimum alveolar pressure (between 7-12 cmH_2O) that maximizes arteriole/venule diameters (**Fig. 5b**), which in turn can minimize the vascular resistance. This finding is consistent with previous literature that has established arterioles and venules as the dominant direct regulators of blood pressure[34]. At an intermediate respiratory pressure, the reduced vascular resistance in arterioles and venules may mean that blood cells are quickly trafficked into or out of the capillary bed. Simultaneously, single capillaries in healthy lung also displayed respiration-circulation coupling. Capillary diameter increased dramatically with increasing vascular pressure (**Fig. 5c**). However, the average diameter was also almost always monotonically decreasing when increasing alveolar pressure higher than 7 cmH_2O. This indicates that alveolar pressures around 7 cmH_2O produce a minimum vascular resistance in capillaries, but that respiration in general does not dominate over vascular pressure in determining capillary diameter. To our knowledge this is the first presentation of a tight coupling between respiration and circulation studied at the single capillary level over the entire surface of a functional lung.

Acute injury is known to significantly remodel the structure of the lung parenchyma. Having characterized respiration-circulation coupling in the uninjured lung, we next probed whether acute injury (modeled by LPS administration) would remodel respiration-circulation function in addition to tissue structure. Acute injury after LPS was characterized by the presence of a large and

inflamed capillary bed at the lung surface (**Fig. 5d**), and reduced size of alveoli across the full breathing cycle. Analysis of capillary diameter with changing alveolar and vascular pressure in the injured area revealed that injured capillaries lost almost all respiration-circulation coupling dynamics. Increasing vascular pressure did little to increase vascular diameter and increasing air pressure did not consistently reduce vascular diameter, as it had in healthy capillaries (**Fig. 5e**). Thus, the presence of acute injury disrupted the ability of the lung to properly modulate local vascular diameter, and blood pressure, which could lead to a reduction in flow and loss of oxygen transport.

The altered respiration-circulation coupling described above may provide insight into neutrophils' mechano-responsiveness to pressure. We observed that populations of neutrophils recruited to a lung infected with bacterial pneumonia migrated faster with increasing vascular pressure (**Fig. 5f**), which was accompanied by an increase in capillary diameter (**Fig. 5g**). However, increasing alveolar pressure in pneumonia lungs did not result in a change in neutrophil speed (**Fig. 5h**), which also did not change the capillary diameters (**Fig. 5i**). This correlation may suggest that changes in vascular diameter and the resulting tensional stresses in the vascular substate are responsible for the changes in neutrophil migration speed, potentially by facilitating binding of neutrophils to the endothelial wall during rolling adhesion[35].

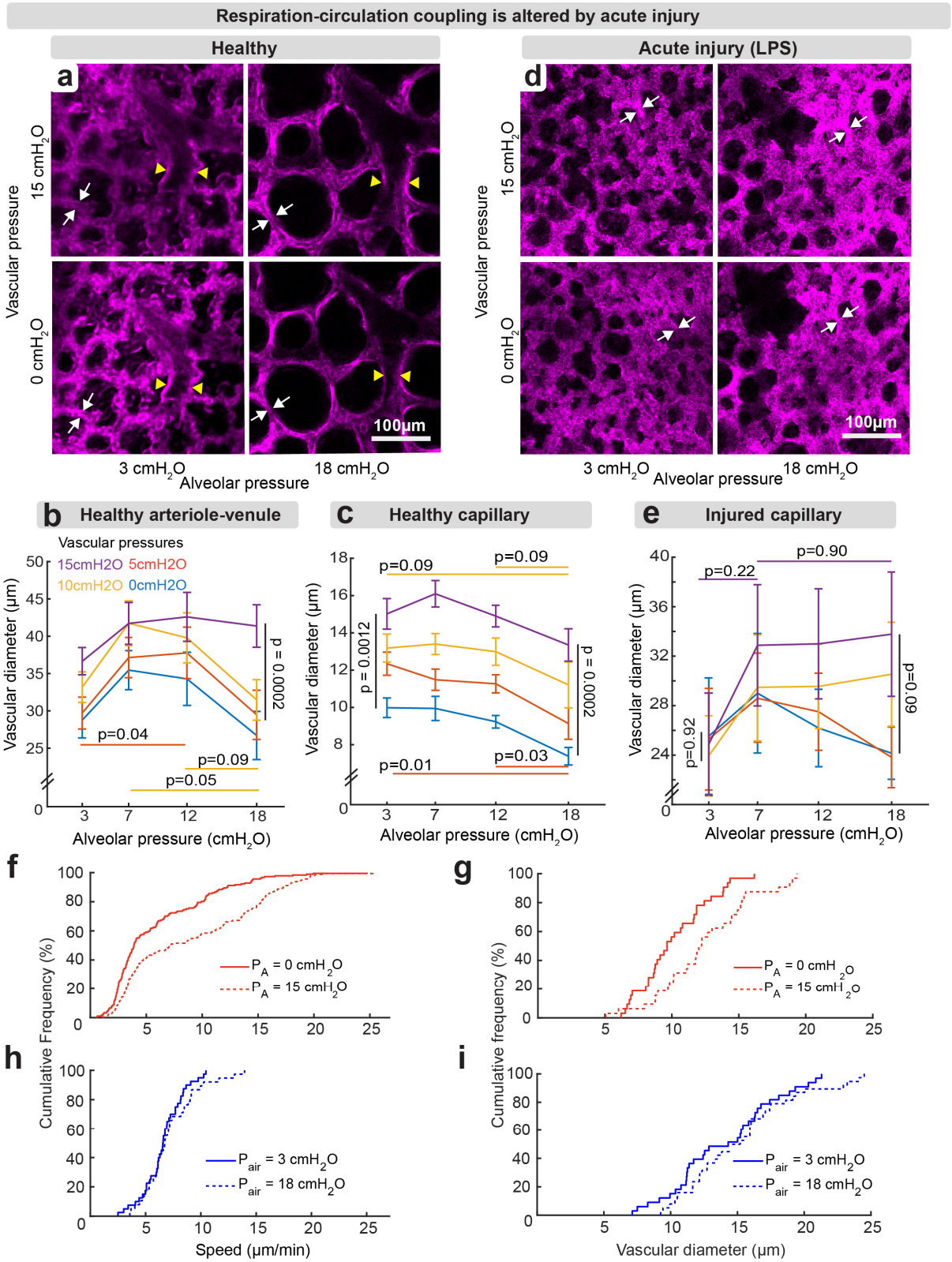

FIGURE 5 | Respiration-circulation coupling in healthy lungs and its disruption by acute injury. (**a**) Representative image of structural changes in the lung associated with variable alveolar and vascular pressures, with measurements of single diameter changes in single lung capillaries (white arrows) and large arterioles (yellow arrows),

which can be tracked in the crystal ribcage across normal respiration-circulation parameters. (**b**) Representative images lung injury after challenge with LPS, showing that single capillaries (white arrows) affected by acute injury (LPS) become inflamed and distend differently for the same pressure range. (**c**) Respiration-circulation coupling trends can be observed by measuring changes in diameter of large, heathy arterioles and (**d**) healthy single capillaries (n = 4 mice), (**e**) and capillaries affected by acute injury (n = 4 mice). (**f**) Neutrophils tend to migrate at faster speeds as vascular pressure measured at the pulmonary artery (PA) increases (n = 2 mice), potentially associated to the increases in vascular diameter (**g**; n = 2 mice). (**h**) Increasing alveolar air pressure does not cause neutrophils to migrate faster (n = 2 mice), and (**i**) similarly changing air pressure has little effect on vascular diameter (n = 2 mice).

Discussion

We have developed the crystal ribcage and demonstrated its capabilities for probing lung (dys)function across nearly the entire surface at the whole-organ, alveolar and cellular scales in real time. Where previous methods are (i) unable to resolve micro-scale features (MRI, CT), (ii) lack temporal dynamics and disrupt the native air-liquid interface (histology), and (iii) compromise respiratory motion (intravital microscopy[1,3]), the crystal ribcage enables imaging of respiratory and circulatory functions down to cellular scale, and preserves the native 3-D and complex architecture and cellular diversity of the lung. We have applied the crystal ribcage to a wide array of pulmonary diseases such as cancer (primary and metastatic), pneumonia, emphysema, and fibrosis (**Fig. 1**). In cancer, we found (i) differential remodeling of alveolar function in nodular vs infiltrative (co-optive) growth pattern, (ii) the earliest stages of tumorigenesis that compromises alveolar respiratory function, and (iii) reduced capillary function around a nodular tumor (**Fig. 2**). In pneumonia, we mapped the spatial heterogeneity of alveolar function at the lobe and alveolar scales and revealed how respiratory and circulatory functions of alveoli and capillaries are altered by inflammation (**Fig. 3**). By modulating vascular pressure in the lung, we found that neutrophils are strongly and reversibly mechano-responsive to vascular pressure in a mouse model of pneumonia and acute lung injury (**Fig. 4**). Lastly, we demonstrated that respiration and circulation are tightly coupled at the capillary level and found that this coupling is eliminated in acute injury (**Fig. 5**). Overall, the crystal ribcage uniquely combines the precise perturbation and intervention capabilities of *in vitro* lung-on-chip models[8,12] with the multiscale and high spatiotemporal imaging of the whole, functional lung in health and disease. This transformative platform opens the door to probing the dynamics of pathogenesis down to the single cell, with potential for discovery of novel mechanisms and targets relevant not only to disease, but also to lung transplantation, development, and aging.

The first iteration of the crystal ribcage, presented here, was designed for the mouse lung to take advantage of the wide range of transgenic and reporter mice available for modeling pulmonary diseases. However, mice models cannot be used to study the effects of gravity on lung (dys)function, such as in ARDS patients[36], and certain diseases such as SARS-CoV-2 are challenging to accurately model in mice. In future work, we will take advantage of the scalability of our fabrication process to develop the rigid crystal ribcage for large animals like pig and transplant-rejected human lungs[37] to probe diseases and therapeutics in a more clinically relevant setting. Additionally, disease models in this study were developed in the *in vivo* mouse on the order of days-weeks, and we probed the (patho)physiology of these lung diseases for 4-6 hours *ex vivo* inside the crystal ribcage. This is a sufficient timescale for studying dynamic events such respiration function, immune cell migration, and circulation dynamics in mouse models. However, recent studies have maintained human lungs up to 24 hours *ex vivo* [38] , pig lungs up to 3 days[39] and

rats up to 7 days[40]. Utilizing these advances[41], we will adapt the crystal ribcage to maintain lung viability for multi-day studies of disease dynamics. Specifically, given that the crystal ribcage enables real-time imaging of lung injury and at the single alveolus level, our platform can be used to design strategies for improving human donor lung preservation over time and push the duration of lung viability *ex vivo*, with impacts on lung transplantation research[42].

While the crystal ribcage supports probing of several lung diseases with parenchymal presentation, deeper imaging could expand the capabilities of our platform. Currently, optical imaging of lungs is depth-limited due to the refraction of light at the many air-liquid interfaces at the alveolar scale[7,8], independent of the properties of the crystal ribcage. Imaging healthy lungs in the crystal ribcage using laser confocal microscopy, two-photon microscopy, and optical coherence tomography, we can resolve healthy lung structure up to one to two alveoli (50-100μm) deep into the tissue. When the airspace is filled with liquid as in pulmonary edema or liquid ventilation strategies, or by solid phase as in lung tumors, the crystal ribcage enables deeper imaging up to 500 μm (**Extended Data Fig. 19**). Lastly, in our present work we have probed the lung respiration mechanics under quasi-static conditions to decouple the effects of tissue viscoelasticity and bulk liquid flow from equilibrium elasticity and constant vascular pressure changes. By using ultrafast volumetric imaging techniques, such as light sheet microscopy (e.g., SCAPE[43]), the crystal ribcage can resolve respiration and circulation dynamics at the "speed of life", i.e. at physiologically relevant respiration and circulation time scales to study the dynamic coupling between circulation and respiration, fast cell-cell communications such as calcium signaling, and quantify viscoelastic properties and energy dissipation at the alveolar level, all in a functioning lung.

Acknowledgements: We thank the Neurophotonics Center at Boston University for their generous support and access to their facility. Adam Coats from the Hoffman lab at the University of Iowa provided the μCT image data sets used to fabricate the crystal ribcage. The research reported in this publication was supported by the Boston University Micro and Nano Imaging Facility and the Office of the Director, National Institutes of Health of the National Institutes of Health under award Number S10OD024993. The content is solely the responsibility of the authors and does not necessarily represent the official views of the National Institute of Health.

Funding: H.T.N. discloses support for the research described in this study from the National Institutes of Health R21EB031332 and DP2HL168562, Beckman Young Investigator Award, Boston University Center for Multiscale and Translational Mechanobiology, and Dean's Catalyst Award, Johnson & Johnson Lung Cancer Initiative, and the American Cancer Society Institutional Fund at Boston University.

Author contributions: R.B., G.N.G. and H.T.N. conceived the project and wrote the manuscript; R.B. developed and validated the crystal ribcages and external devices suite, established transgenic mouse colonies, analyzed alveolar function data; G.N.G. conducted the lung extraction and imaging, generated experimental mice, analyzed circulatory function data; L.S. analyzed neutrophil mechano-responsiveness data; D.S. analyzed alveolar and capillary function data, and maintained animal colony; R.L. developed strain analysis algorithm; J.M. developed custom hardware for crystal ribcage and analyzed alveolar function data; C.E. developed deformable crystal ribcage; B.H. generated lobar pneumonia model; J.L. generated fibrosis model; K.R. and S. Z. cultured cancer cells; S.S.Z. fabricated fluorescent polyacrylamide beads; J.J. assisted in surgical technique for *in situ* lung imaging; R.P. generated LPS model induction; K.T. provided transgenic MPR8-Cre^{+} mouse; G.L., J.P.M. and B.S. contributed to discussion on crucial aspects of the project; H.T.N. supervised the project and provided guidance on experimental design, data collection, data interpretation and writing of the manuscript.

Competing interests: Authors declare that they have no competing interests.

Data availability: All data are available in the main text or the Extended Data section. Raw data and code for analysis are available upon request. Correspondence and request for code, raw data and materials should be addressed to H.T.N.

References

1 Entenberg, D. *et al.* A permanent window for the murine lung enables high-resolution imaging of cancer metastasis. *Nat Methods* **15**, 73-80 (2018). https://doi.org:10.1038/nmeth.4511

2 Headley, M. B. *et al.* Visualization of immediate immune responses to pioneer metastatic cells in the lung. *Nature* **531**, 513-517 (2016). https://doi.org:10.1038/nature16985

3 Looney, M. R. *et al.* Stabilized imaging of immune surveillance in the mouse lung. *Nat Methods* **8**, 91-96 (2011). https://doi.org:10.1038/nmeth.1543

4 Ueki, H., Wang, I. H., Zhao, D., Gunzer, M. & Kawaoka, Y. Multicolor two-photon imaging of in vivo cellular pathophysiology upon influenza virus infection using the two-photon IMPRESS. *Nat Protoc* **15**, 1041-1065 (2020). https://doi.org:10.1038/s41596-019-0275-y

5 Westphalen, K. *et al.* Sessile alveolar macrophages communicate with alveolar epithelium to modulate immunity. *Nature* **506**, 503-506 (2014). https://doi.org:10.1038/nature12902

6 Borriello, L. *et al.* Primary tumor associated macrophages activate programs of invasion and dormancy in disseminating tumor cells. *Nat Commun* **13**, 626 (2022). https://doi.org:10.1038/s41467-022-28076-3

7 Lefrancais, E. *et al.* The lung is a site of platelet biogenesis and a reservoir for haematopoietic progenitors. *Nature* **544**, 105-109 (2017). https://doi.org:10.1038/nature21706

8 Hassell, B. A. *et al.* Human Organ Chip Models Recapitulate Orthotopic Lung Cancer Growth, Therapeutic Responses, and Tumor Dormancy In Vitro. *Cell Rep* **21**, 508-516 (2017). https://doi.org:10.1016/j.celrep.2017.09.043

9 Haudebourg, A. F. *et al.* Respiratory Mechanics of COVID-19- versus Non-COVID-19-associated Acute Respiratory Distress Syndrome. *Am J Respir Crit Care Med* **202**, 287-290 (2020). https://doi.org:10.1164/rccm.202004-1226LE

10 Lederer, D. J. & Martinez, F. J. Idiopathic Pulmonary Fibrosis. *N Engl J Med* **378**, 1811-1823 (2018). https://doi.org:10.1056/NEJMra1705751

11 Suki, B. *et al.* Emphysema and mechanical stress-induced lung remodeling. *Physiology (Bethesda)* **28**, 404-413 (2013). https://doi.org:10.1152/physiol.00041.2013

12 Huh, D. *et al.* Reconstituting organ-level lung functions on a chip. *Science* **328**, 1662-1668 (2010). https://doi.org:10.1126/science.1188302

13 Hall, J. E. *Guyton and hall textbook of medical physiology*. 14. edn, (Elsevier, 2020).

14 Collaborators, G. B. D. R. T. C. Global, regional, and national burden of respiratory tract cancers and associated risk factors from 1990 to 2019: a systematic analysis for the Global Burden of Disease Study 2019. *Lancet Respir Med* **9**, 1030-1049 (2021). https://doi.org:10.1016/S2213-2600(21)00164-8

15 Stella, G. M., Kolling, S., Benvenuti, S. & Bortolotto, C. Lung-Seeking Metastases. *Cancers (Basel)* **11** (2019). https://doi.org:10.3390/cancers11071010

16 Seano, G. *et al.* Solid stress in brain tumours causes neuronal loss and neurological dysfunction and can be reversed by lithium. *Nat Biomed Eng* **3**, 230-245 (2019). https://doi.org:10.1038/s41551-018-0334-7

17 Eefsen, R. L. *et al.* Growth pattern of colorectal liver metastasis as a marker of recurrence risk. *Clin Exp Metastasis* **32**, 369-381 (2015). https://doi.org:10.1007/s10585-015-9715-4

18 Cuypers, A., Truong, A. K., Becker, L. M., Saavedra-Garcia, P. & Carmeliet, P. Tumor vessel co-option: The past & the future. *Front Oncol* **12**, 965277 (2022). https://doi.org:10.3389/fonc.2022.965277
19 Conklin, M. W. *et al.* Aligned collagen is a prognostic signature for survival in human breast carcinoma. *Am J Pathol* **178**, 1221-1232 (2011). https://doi.org:10.1016/j.ajpath.2010.11.076
20 Provenzano, P. P. *et al.* Collagen reorganization at the tumor-stromal interface facilitates local invasion. *BMC Med* **4**, 38 (2006). https://doi.org:10.1186/1741-7015-4-38
21 Garcia-Mendoza, M. G. *et al.* Neutrophils drive accelerated tumor progression in the collagen-dense mammary tumor microenvironment. *Breast Cancer Res* **18**, 49 (2016). https://doi.org:10.1186/s13058-016-0703-7
22 Nia, H. T., Munn, L. L. & Jain, R. K. Physical traits of cancer. *Science* **370** (2020). https://doi.org:10.1126/science.aaz0868
23 Baskaran, J. P. *et al.* Cell shape, and not 2D migration, predicts extracellular matrix-driven 3D cell invasion in breast cancer. *APL Bioeng* **4**, 026105 (2020). https://doi.org:10.1063/1.5143779
24 Thibault, H. B. *et al.* Noninvasive assessment of murine pulmonary arterial pressure: validation and application to models of pulmonary hypertension. *Circ Cardiovasc Imaging* **3**, 157-163 (2010). https://doi.org:10.1161/CIRCIMAGING.109.887109
25 Alexandrakis, G. *et al.* Two-photon fluorescence correlation microscopy reveals the two-phase nature of transport in tumors. *Nat Med* **10**, 203-207 (2004). https://doi.org:10.1038/nm981
26 Murdoch, D. R. & Howie, S. R. C. The global burden of lower respiratory infections: making progress, but we need to do better. *Lancet Infect Dis* **18**, 1162-1163 (2018). https://doi.org:10.1016/S1473-3099(18)30407-9
27 Passegue, E., Wagner, E. F. & Weissman, I. L. JunB deficiency leads to a myeloproliferative disorder arising from hematopoietic stem cells. *Cell* **119**, 431-443 (2004). https://doi.org:10.1016/j.cell.2004.10.010
28 Lefrancais, E., Mallavia, B., Zhuo, H., Calfee, C. S. & Looney, M. R. Maladaptive role of neutrophil extracellular traps in pathogen-induced lung injury. *JCI Insight* **3** (2018). https://doi.org:10.1172/jci.insight.98178
29 Quinton, L. J., Walkey, A. J. & Mizgerd, J. P. Integrative Physiology of Pneumonia. *Physiol Rev* **98**, 1417-1464 (2018). https://doi.org:10.1152/physrev.00032.2017
30 Domscheit, H., Hegeman, M. A., Carvalho, N. & Spieth, P. M. Molecular Dynamics of Lipopolysaccharide-Induced Lung Injury in Rodents. *Front Physiol* **11**, 36 (2020). https://doi.org:10.3389/fphys.2020.00036
31 Mitchell, M. J., Lin, K. S. & King, M. R. Fluid shear stress increases neutrophil activation via platelet-activating factor. *Biophys J* **106**, 2243-2253 (2014). https://doi.org:10.1016/j.bpj.2014.04.001
32 Huse, M. Mechanical forces in the immune system. *Nat Rev Immunol* **17**, 679-690 (2017). https://doi.org:10.1038/nri.2017.74
33 Whipp, B. J. & Ward, S. A. Cardiopulmonary coupling during exercise. *J Exp Biol* **100**, 175-193 (1982). https://doi.org:10.1242/jeb.100.1.175
34 Mulvany, M. J. & Aalkjaer, C. Structure and function of small arteries. *Physiol Rev* **70**, 921-961 (1990). https://doi.org:10.1152/physrev.1990.70.4.921

35 Phillipson, M. & Kubes, P. The neutrophil in vascular inflammation. *Nat Med* **17**, 1381-1390 (2011). https://doi.org:10.1038/nm.2514
36 Guerin, C. *et al.* Prone positioning in severe acute respiratory distress syndrome. *N Engl J Med* **368**, 2159-2168 (2013). https://doi.org:10.1056/NEJMoa1214103
37 Hozain, A. E. *et al.* Xenogeneic cross-circulation for extracorporeal recovery of injured human lungs. *Nat Med* **26**, 1102-1113 (2020). https://doi.org:10.1038/s41591-020-0971-8
38 Cardenes, N. *et al.* Human ex vivo lung perfusion: a novel model to study human lung diseases. *Sci Rep* **11**, 490 (2021). https://doi.org:10.1038/s41598-020-79434-4
39 Ali, A. *et al.* Successful 3-day lung preservation using a cyclic normothermic ex vivo lung perfusion strategy. *EBioMedicine* **83**, 104210 (2022). https://doi.org:10.1016/j.ebiom.2022.104210
40 Petersen, T. H., Calle, E. A., Colehour, M. B. & Niklason, L. E. Bioreactor for the long-term culture of lung tissue. *Cell Transplant* **20**, 1117-1126 (2011). https://doi.org:10.3727/096368910X544933
41 Loor, G. *et al.* Prolonged EVLP Using OCS Lung: Cellular and Acellular Perfusates. *Transplantation* **101**, 2303-2311 (2017). https://doi.org:10.1097/TP.0000000000001616
42 Kesseli, S. J., Davis, R. P. & Hartwig, M. G. Commentary: Making lungs great again-introducing new modifications to the Toronto ex vivo lung perfusion protocol. *J Thorac Cardiovasc Surg* **161**, 1974-1975 (2021). https://doi.org:10.1016/j.jtcvs.2020.08.016
43 Voleti, V. *et al.* Real-time volumetric microscopy of in vivo dynamics and large-scale samples with SCAPE 2.0. *Nat Methods* **16**, 1054-1062 (2019). https://doi.org:10.1038/s41592-019-0579-4
44 Muzumdar, M. D., Tasic, B., Miyamichi, K., Li, L. & Luo, L. A global double-fluorescent Cre reporter mouse. *Genesis* **45**, 593-605 (2007). https://doi.org:10.1002/dvg.20335
45 Kassie, F., Matise, I., Negia, M., Upadhyaya, P. & Hecht, S. S. Dose-dependent inhibition of tobacco smoke carcinogen-induced lung tumorigenesis in A/J mice by indole-3-carbinol. *Cancer Prev Res (Phila)* **1**, 568-576 (2008). https://doi.org:10.1158/1940-6207.CAPR-08-0064
46 Mizgerd, J. P., Scott, M. L., Spieker, M. R. & Doerschuk, C. M. Functions of IkappaB proteins in inflammatory responses to Escherichia coli LPS in mouse lungs. *Am J Respir Cell Mol Biol* **27**, 575-582 (2002). https://doi.org:10.1165/rcmb.2002-0015OC
47 Barker, K. A. *et al.* Lung-resident memory B cells protect against bacterial pneumonia. *J Clin Invest* **131** (2021). https://doi.org:10.1172/JCI141810
48 Caporarello, N. *et al.* Dysfunctional ERG signaling drives pulmonary vascular aging and persistent fibrosis. *Nat Commun* **13**, 4170 (2022). https://doi.org:10.1038/s41467-022-31890-4
49 Suki, B., Bartolak-Suki, E. & Rocco, P. R. M. Elastase-Induced Lung Emphysema Models in Mice. *Methods Mol Biol* **1639**, 67-75 (2017). https://doi.org:10.1007/978-1-4939-7163-3_7
50 Vanderpool, R. R. & Chesler, N. C. Characterization of the isolated, ventilated, and instrumented mouse lung perfused with pulsatile flow. *J Vis Exp* (2011). https://doi.org:10.3791/2690
51 Kizhakke Puliyakote, A. S. *et al.* Morphometric differences between central vs. surface acini in A/J mice using high-resolution micro-computed tomography. *J Appl Physiol (1985)* **121**, 115-122 (2016). https://doi.org:10.1152/japplphysiol.00317.2016

52 Thiesse, J. *et al.* Lung structure phenotype variation in inbred mouse strains revealed through in vivo micro-CT imaging. *J Appl Physiol (1985)* **109**, 1960-1968 (2010). https://doi.org:10.1152/japplphysiol.01322.2009

53 Vasilescu, D. M. *et al.* Stereological assessment of mouse lung parenchyma via nondestructive, multiscale micro-CT imaging validated by light microscopic histology. *J Appl Physiol (1985)* **114**, 716-724 (2013). https://doi.org:10.1152/japplphysiol.00855.2012

54 Schulte, H., Muhlfeld, C. & Brandenberger, C. Age-Related Structural and Functional Changes in the Mouse Lung. *Front Physiol* **10**, 1466 (2019). https://doi.org:10.3389/fphys.2019.01466

55 Gokaltun, A., Kang, Y. B. A., Yarmush, M. L., Usta, O. B. & Asatekin, A. Simple Surface Modification of Poly(dimethylsiloxane) via Surface Segregating Smart Polymers for Biomicrofluidics. *Sci Rep* **9**, 7377 (2019). https://doi.org:10.1038/s41598-019-43625-5

56 Allen, M., Poggiali, D., Whitaker, K., Marshall, T. R. & Kievit, R. A. Raincloud plots: a multi-platform tool for robust data visualization. *Wellcome Open Res* **4**, 63 (2019). https://doi.org:10.12688/wellcomeopenres.15191.1

57 Heinrich, M. P., Jenkinson, M., Brady, M. & Schnabel, J. A. MRF-based deformable registration and ventilation estimation of lung CT. *IEEE Trans Med Imaging* **32**, 1239-1248 (2013). https://doi.org:10.1109/TMI.2013.2246577

Methods

Mice

Mice were housed and bred under pathogen–free conditions at the Boston University Animal Science Center. All experiments conformed to ethical principles and guidelines under protocols approved by the Boston University Institutional Animal Care and Use Committee. We used 6- to 12-week-old male and female mice for the experimental procedures. Female FVB mice aged 6-8 weeks (JAX #001800, Jackson Labs, ME) were purchased. A breeding pair of transgenic B6.129(Cg)-Gt(ROSA)26Sortm4(ACTB-tdTomato,-EGFP)Luo/J (JAX #007676, Jackson lab, ME)[44], hereafter referred to as mTmG, was purchased to start a colony and was the primary source of all animals for the experiments. Male neutrophil reporter mice B6.Cg-Tg(S100A8-cre,-EGFP)1Ilw/J (JAX #021614)[27] were purchased from JAX and crossed with in-house homozygous mTmG females to breed MRP8-mTmG mice that were used for neutrophil migration dynamics.

Metastatic cancer model

E0771-H2B-dendra2 mouse cancer cells or MCa-M3C-H2B-dendra2 (both gifts from Rakesh Jain) were used to model breast cancer metastasis to the lung in mTmG and FVB mice, respectively. Cells were cultured in DMEM (Corning) plus 10% fetal bovine serum (Gibco) plus 1% penicillin/streptomycin (Gibco). Cells were harvested at ~80% confluency, washed twice with phosphate buffered saline (PBS), counted, and resuspended in DMEM prior to tail vein injection into mice at a concentration of 2 million per 300uL complete medium. All cell lines tested negative for mycoplasma (Mycoalert Plus Mycoplasma Detection Kit, Lonza, Allendale, NJ), and authenticated before use by IDEXX laboratories (North Grafton, MA). Mice injected with E0771-H2B-dendra2 were sacrificed on days 5-7 post injection for microscopy of mature nodules. Mice injected with MCa-M3C-H2B-dendra2 were sacrificed on days 10-14 for microscopy of mature nodules. For single cell deformation studies, E0771-H2B-dendra2 cells were plasma membrane labeled with 1,1'-Dioctadecyl-3,3,3',3'-Tetramethylindocarbocyanine, 4-Chlorobenzene Sulfonate Salt (DiD, Invitrogen) before imaging, then washed twice with complete cell culture medium and injected intracardiac into the mouse at a concentration of 6 million per 300uL solution.

Primary cancer model

We induced tumorigenesis in 6-week female A/J mice as described previously[45]. Briefly, we treated the mice with a cocktail of Benzo[a]pyrene (BaP) (B1760, Millipore-Sigma, USA) (0.5 mg/dose) and 4-(Methylnitrosoamino)-1-(3-pyridinyl)-1-butanone (NNK) (78013, Millipore-Sigma) (0.41 mg/dose) were dissolved in cotton oil (C7767, Millipore-Sigma) and delivered to the back of the tongue using a metal 20G feeding tube. The mice were dosed twice per week for 4 weeks to give them a total of 8 doses and then sacrificed at 20 weeks to prepare the tissue for imaging in the crystal ribcage.

LPS acute inflammation model

mTmG mice were treated with 100 µg *Escherichia coli* (*E. coli,* serotype O55:B5, Sigma-Aldrich) lipopolysaccharide LPS diluted to 100 ug/60 µL in PBS via intratracheal injection using an angio-catheter as previously described[46], to model acute injury. Mice were sacrificed 3-4 hours post induction for microscopy of the acutely injured tissue in the *ex vivo* lung.

Bacterial pneumonia model

We induced bacterial pneumonia in mice as previously described[47]. Briefly, *S. pneumoniae* serotype 3 (Sp3) (ATCC; Manassas, VA) was cultured on plates of BBL Trypticase Soy Agar with 5% sheep blood (BD Trypticase Soy Agar II) (BD Biosciences) in a 37°C humidified 5% CO2 environment for 10-11 hours and diluted in 0.9% sodium chloride to the desired optical density. Mice were anesthetized using a ketamine/xylazine cocktail (100 and 10 mg/kg, respectively) and approximately two million CFU in 50 µL were instilled into the left lung lobe via the left bronchus, accessed through the surgically exposed trachea.

Pulmonary fibrosis model

Bleomycin was delivered to the lungs as previously described[48]. Mice were anesthetized with ketamine/xylazine cocktail (100 and 10 mg/kg, respectively) and injected intraperitoneally. About 1 U/Kg bleomycin (APP Pharmaceutical, LCC Schaumburg, IL, USA) was intratracheally delivered using a 30G insulin syringe. Mice were sacrificed for microscopy of fibrotic injuries 13-14 days after injection.

Elastase induced COPD model

COPD was induced in mTmG mice by digesting the elastase in the lung using porcine pancreatic elastase (PPE) (EC134 Elastin Product Company Inc., Owensville, MO). A previously published protocol was followed for single dose treatment[49], briefly 6 IU PPE was dissolved in 100 µL saline and delivered to the mouse (23-25 g). The solution was instilled at the back of the tongue after anesthetizing the mouse and suspending it vertically after which it was allowed to recover normally. Mice were sacrificed at 21 days from instillation to prepare the lung inside the crystal ribcage for imaging.

Lung preparation

Isolated mouse lungs were ventilated through a tracheal cannula and perfused through two cannulas inserted into the pulmonary artery (PA) and left atrium as previously described[50]. Perfusions included whole blood, cellular, or acellular media containing fluorescent labels for vascular lumens and circulating cells. After cannulation, the lung-heart bloc was placed into the crystal ribcage for microscopy under controlled ventilation/circulation parameters. The lung was ventilated *ex vivo* using a (Kent Physiosuite Mouse ventilator, Kent Scientific) or held at static alveolar pressure using an air-filled vinyl tube submerged in a water column. Perfusion pressure was controlled using a 60 mL reservoir containing the perfusate medium (serum-free RPMI, Gibco) suspended at different hydrostatic heights above the height of the lung.

***In situ* lung imaging**

Mice were anesthetized as described above and ventilated through a tracheal cannula. The mouse was sacrificed at this point ensuring the lungs did not collapse but maintain a positive end expiratory pressure (PEEP) of 5-7 cmH_2O. The skin and fascia were dissected away and then the intercostal muscles between the ribs was carefully separated under a stereomicroscope till the underlying ribcage pleura was visible. A 2mm x 3mm retaining clamp was inserted in the cleared section to prevent the leftover tissue strands blocking the opening. The PEEP on the lung was altered to confirm that the lung-maintained contact with the internal pleural membrane and that the lung was responsive to pressure changes. The mouse chest carcass was angled upwards for imaging.

Lung microscopy

Prepared *ex vivo* lungs inside the crystal ribcage were imaged using an inverted laser-scanning confocal microscope (Olympus FV 3000) under objective magnifications of 1.25x, 10x, and 20x, with environmental temperature control set to 37°C using Fluoview acquisition software. Additionally, lungs were imaged using an upright Nikon fluorescent stereomicroscope, a ThorLabs upright optical coherence tomography probe and an upright Bruker two-photon microscope equipped with a 16x water immersion objective. Microscopy data was visualized using FIJI and MATLAB2021b.

Mouse ribcage 3-D object creation

Previously recorded pressure controlled µCT scans of C57B/6 and AJ mice chest cavities were obtained from the Hoffman group at the University of Iowa[51-53]. FVB mouse chest scans were performed at the Boston University Micro-CT imaging facility. These scans were segmented in MATLAB (v. R2019b Mathworks, Natick MA) using a custom algorithm and user defined regions of interest to obtain a coarse 3D object that represented the mouse chest cavity including a small section of the trachea. This coarse 3D binary object was refined and re-meshed in Meshmixer (Autodesk) to remove any sharp edges and make a stereolithography (STL) object. The Meshmixer files were imported into Solidworks 2019 (Dassault systems, France) to add registration features prior to 3D printing. The model was made age-specific by scaling the binary object by mouse lung volume reported by age[54] (**Extended Data Fig. 1**). The final STL file was printed using FormLabs (Somerville, MA) clear resin on a Form3 printer and additionally post-cured for 30 minutes. The final 3D printed insert was washed and polished to remove any layer lines and obtain a high gloss finish on the surface.

PDMS ribcage fabrication

The 3D printed lung insert was used to make a negative mold by embedding it in a soft silicone-based elastomer called Ecoflex 00-30 (Smooth-On Inc, Macungie PA) under vacuum for 5 hours. Post curing the 3D insert was removed to obtain a smooth exact negative mold. The internal surface of the mold was coated with a thin layer of PDMS to completely seal it from air and make the internal geometry rigid. The negative space was slowly filled with a casting sugar solution that was kept liquid at ~140˚C. The sugar filled mold was degassed in the oven for over an hour to remove any trapped air bubbles in the sugar, cured by cooling over 2 hours at room temperature, and then gently removed by deforming the soft silicone mold. Polymethyldisiloxane (PDMS) was mixed in a standard 10:1 monomer to crosslinker ratio and gradually poured over the sugar mold, completely covering the surface, and then set to partially cure at ~50˚C for 25-30 minutes. This was repeated five times after which it was left to cure for 12-18 hours at ~50˚C in a dehydrating oven. The cast PDMS was positioned in a 3D printed crystal ribcage support and attached with dabs of glue. The assembly was then left in lukewarm water for 2-3 hours to dissolve the cast sugar to obtain the PDMS crystal ribcage (**Extended Data Fig. 1**).

Polystyrene ribcage fabrication

The 3D printed insert was positioned over a miniature dental thermoforming device. A 0.7mm clear polystyrene sheet was fed into the device and allowed to heat before it was pulled over the 3D printed insert while applying a vacuum to remove any trapped air between the mold and the polystyrene. The heat and vacuum were turned off and the formed polystyrene was removed from

over the mold using compressed air. This rigid crystal ribcage was fitted into a support neck and fused by friction welding and using cyanoacrylate glue (**Extended Data Fig. 1**).

Crystal ribcage surface treatment

Both rigid and deformable crystal ribcage surfaces have native hydrophobic surfaces which were engineered to be hydrophilic. The polystyrene surface was treated with oxygen plasma using a Harrick Plasma Cleaner, where the crystal ribcage was subjected to a vacuum of 800-900 mTorr and then plasma treatment at medium power for 2 minutes. The internal surface of the PDMS crystal ribcage was treated with a 1% PDMS-PEG Block Copolymer () and allowed to cure to improve hydrophilicity as shown previously[55].

Versatile microscopy arm

We developed two custom microscopy arms using commercially available photography brackets to allow both 3- and 6-degrees of freedom to orient the crystal ribcage with available upright (fluorescent stereomicroscope, multi-photon microscope, optical coherence tomography) or inverted microscopes (laser scanning confocal microscope) (**Extended Data Fig. 6**). We successfully tested our mounting arm to image the lung surface with the above microscopes and with a wide range of objective power, ranging from 1.25x (lobe-scale), 10x (alveolar-scale), and 40x (subcellular-scale) imaging of the same lung.

Ventilation pressure and flow sensor calibration

Ventilation pressure sensors SSDRRV100MDAA5 (Honeywell Inc.) were rated to measure between ±100 cmH_2O with a 0-5 V linearly scaled output. The pressure sensor was calibrated prior to every experiment with a simple water column between 0-10 cmH_2O and the calibration value was used to scale the raw voltage into pressure values in real-time. The flow sensor was calibrated one-time when it was assembled using a 3D printed constriction and SSDRRV010MDAA5 (Honeywell Inc.) differential ±10 cmH_2O linearly scaled pressure sensor. The obtained voltage-flow curve which was fitted to a reflected power curve to obtain the flow values in ml/min for a given change in resistance read across the sensor. All sensor readings were scaled to real units using an Arduino and custom MATLAB functions to display in real-time.

Perfusion pressure and flow sensor calibration

Perfusion was measured with 26PCAFG6G (Honeywell Inc.) that were rated between 0 to 1 PSI unamplified gauge pressure sensors. The pressure sensor was read into an HX711 analog to digital converter before being read on an onboard Arduino Uno. The scaled digital values were calibrated against a known water column between 0-10 cmH_2O prior to every experiment. The perfusion flow was measured using a small form factor Sensirion SLF-1300F liquid flow sensor. The sensor comes factory calibrated for DI water and 70% ethanol. It was calibrated for different perfusates by linearly scaling the sensor reading with a known syringe pump driven flow prior to the experiment. All sensor readings were scaled to real units using an Arduino and custom MATLAB functions to display them in real-time.

Alveolar diameter measurement

Microscopy images recorded with a 10x objective and an additional 1.5x optical zoom were loaded into FIJI-ImageJ and sum-wise projected in the z-direction for all pressure conditions. Alveoli

common to all pressures were annotated prior to making measurements. The mean alveolar diameter was calculated by recording 2 length values between anatomical features that were diametrically opposite to each other. The mean lengths were recorded for all corresponding alveoli at different pressures. These measurements were compiled in MATLAB R2021b to make raincloud plots[56] and compute group-wise statistics.

Alveolar septum strain calculation

We used a previously published deformable registration algorithm, deedsBCV[57] to autonomously determine the displacement map between images of the lung tissue at different inflation pressures, here alveolar pressures of 7 and 12 cmH_2O. Subsequently use a custom algorithm to compute the strain map (**Extended Data Fig. 10-11**). While finite difference methods could also be applied to obtain the displacement gradient it is subject to noise which can obscure the signal. A cubic smoothing spline was used to approximate the displacement map and evaluate its gradient derivative to then directly calculate the canonical strain tensors (**Extended Data Fig. 12**), this method gives us a displacement gradient continuous in its second derivatives which prevents obscuring the true signal in the noise. We first validated the obtained displacement maps by applying known displacements to images to register them and compute the strain. We then validated the effect of the smoothing spline on the original and target images to ensure accurate registration between them by using multiple kernel sizes to ensure that the final registered image matches the target image. The final strain computation algorithm was then validated for known synthetic displacement maps (**Extended Data Fig. 15**) to ensure no fundamental errors existed between the mathematical ground truth and image-based strain estimation.

Single cell measurement

Microscopy images recorded with a 10x objective with a 4x zoom or 20x objective with 4x zoom were loaded into FIJI-ImageJ for all pressure conditions. The maximum plane of the cell was identified by a user and then a freehand trace of the shape of the cell was traced around the cell. Shape parameters including the maximum and minimum Feret diameters were reported by FIJI for every annotation and compiled in MATLAB R2021b to perform statistical comparisons between the Feret ratio (**Extended Data Fig. 13**).

Perfusion and vascular transport

Mouse lungs were perfused with serum-free RPMI at 37°C. To model small molecule drug transport, 50 µL of Cascade Blue dextran (10 kDa, Molecular Probes) or Cascade Blue hydrazide trisodium salt (500 Da, Invitrogen) were injected into the perfusion tubing upstream of the pulmonary artery cannula at a concentration of 10 mg/ml over approximately 1 second. Vascular dynamics were imaged over time using a laser-scanning confocal microscope (Olympus FV3000). Post-processing of vascular transport data was performed in MATLAB R2021b. Microscopy recording channels corresponding to impulse bolus injection were down sampled to a mesh grid with single pixel dimensions on the scale of a single alveolus (approximately 50µm). Intratumor regions were segmented based on the presence of fluorescently labeled tumor cells. Within the extratumor regions, the peri-tumor region was thresholded from regions far from the tumor based on a reduction of bolus intensity threshold. Sp3 infected areas were segmented based on the presence of fluorescently labeled neutrophils. Time series of dye intensity was normalized to the maximum mean intensity of each video (normalized maximum intensity). The duration of dye intensity greater than 50% of the normalized maximum intensity was calculated (T_{50}). The time

from initial increase in pixel intensity time series to the normalized maximum intensity was calculated (T_{max}). Step bolus injections for tumor diffusion were processed in ImageJ to obtain dye intensity intratumor and normalized to baseline intensity measured within the vasculature.

Mathematical model of diffusion

Fick's second law of diffusion governs the spatiotemporal dynamics of diffusion of a particular solute through a given solvent. The law states that the time derivative of the concentration of solute at a specific location is proportional to the Laplacian of its concentration at the same position.

$$(1)\ \frac{\partial \phi}{\partial t} = D\Delta\phi$$

For a ball of radius a initially containing solute of constant concentration C_0 and bounded by a sphere perpetually maintained at constant concentration C_1, the concentration within the ball evolves, according to this law, as a function of radial distance and time :

$$(2)\ C(r,t) = C_1 + (C_1 - C_0)\frac{2a}{\pi r}\sum_{n=1}^{\infty}\frac{(-1)^n}{n} sin\,\frac{n\pi r}{a}\, exp\,(-Dn^2\pi^2 t/a^2)$$

where D is the diffusion coefficient of the solute through the solvent. By integrating this concentration over an equatorial cross section of finite thickness, we can determine the total mass of solute within this cross section as a function of time. This leads to the expression

$$(3)\ M(t) = \iiint_V C(r,t)dV$$

$$(4)\ M(t) = \iint_A C(r,t)LdA$$

$$(5)\ M(t) = \pi a^2 L[C_1 - 8(C_1 - C_0)\sum_{n\,\in\,\{2k-1\,|k\,\in\mathbb{N}\}}\frac{1}{(n\pi)^2}\, exp\,(-D(n\pi)^2 t/a^2)]$$

This last equation has a single unknown parameter, the diffusion coefficient.

In our experiments, if we assume that the intensity of the channel is directly proportional to the concentration, then we can take a unit change in intensity as our unit of concentration. It is then straightforward to compute this same quantity over a cross-section of the tumor from imaging data of the dye channel. This enables us to directly apply the previous model to the integral of the intensity of the dye channel inside the tumor.

By minimizing the squared error between the model and the dataset as a function of the diffusion coefficient, we finally recover the maximum likelihood estimate of the diffusion coefficient under the assumption of Gaussian noise.

Cell tracking for neutrophil migration

Post-processing of neutrophil migration data was performed in MATLAB2021b. Multi-channel recordings from microscopy were stabilized and single neutrophil centroids were computed per frame to obtain corresponding position and speed information. Persistence was calculated as the total displacement divided by contour length of the path. Where relevant, migration through the intravascular space was defined as movement confined within the vasculature, intra-alveolar as

movement within alveolar spaces, and interstitial as those crossing between vascular and alveolar spaces. Neutrophil shape was segmented using an intensity threshold and the *regionprops* function was used to compute aspect ratio and circularity.

Statistical analyses

All experiments were performed at least twice in separate mice to generate biologically independent samples. Data are presented as mean ± standard error of the mean (S.E.M.). All statistics were calculated as a two-tailed Student's t-test to determine significance or p-values between groups of data. All p-values < 0.1 are reported on figures for the users to observe statistical trends of data. Statistical analyses were performed in MATLAB2021b.

Extended Data

Extended Data Movies

Movies are in the following Google Drive folder and are included in the online submission:

https://drive.google.com/drive/folders/1TE0RRUuYl1keVg7bQ9KDGHC1T4BqGlYZ?usp=sharing

Extended Data Movie 1 | Functional ex vivo lung inside rigid polystyrene crystal ribcage

Extended Data Movie 2 | Functional ex vivo lung inside deformable PDMS crystal ribcage

Extended Data Movie 3 | Imaging functional lung with laser scanning confocal microscope

Extended Data Movie 4 | Crystal ribcage provides stable imaging surface for ventilated lung

Extended Data Movie 5 | Functional lung with nodular tumors imaged from apex to base at alveolar resolution using OCT through crystal ribcage

Extended Data Movie 6 | Metastatic cancer cells remodel capillaries

Extended Data Movie 7 | Vascular dye transport imaged at alveolar resolution in health and disease using crystal ribcage

Extended Data Movie 8 | Neutrophil migration speed increases with higher vascular pressure

Extended Data Movie 9 | Neutrophil extravasation and migration imaged through crystal ribcage

Extended Data Figures

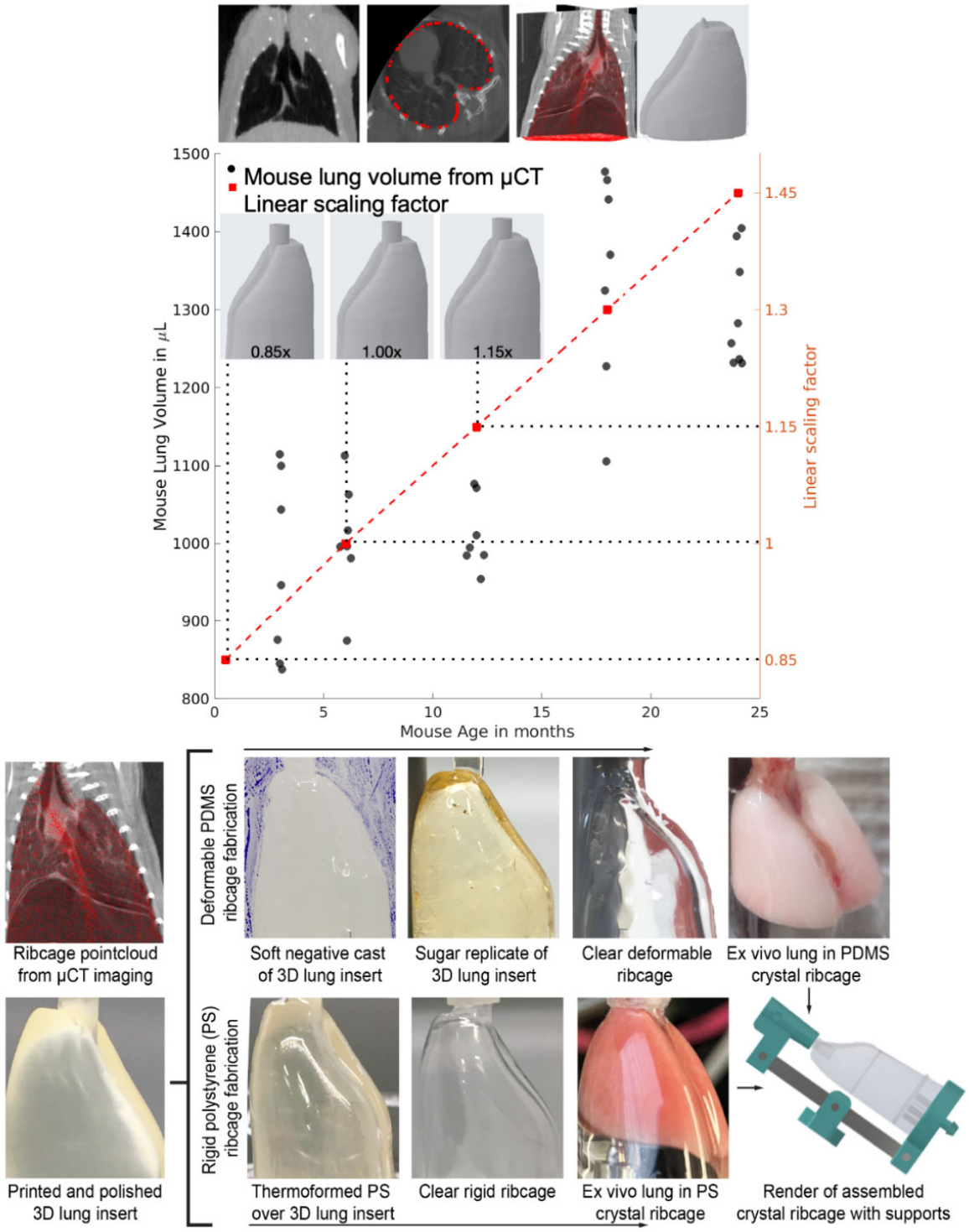

Extended Data Figure 1 | Mouse strain specific µCT informed 3D molds scaled by age and fabrication of crystal ribcages. Recreating mouse ribcage geometry from µCT data, here shown for C57/B6 mice. Top: Sagittal view of mouse chest with fully inflated lung (dark region), distribution of axial control points to recapitulate ribcage cross-section and comparison of reconstructed geometry overlaid on sagittal and coronal µCT slices. Lung volume variation with age was normalized against the mean volume at 3 months to construct a linear fit for scaling 3D lung inserts by age. 3D printed models were used to make both PDMS and polystyrene crystal ribcages in two independent processes.

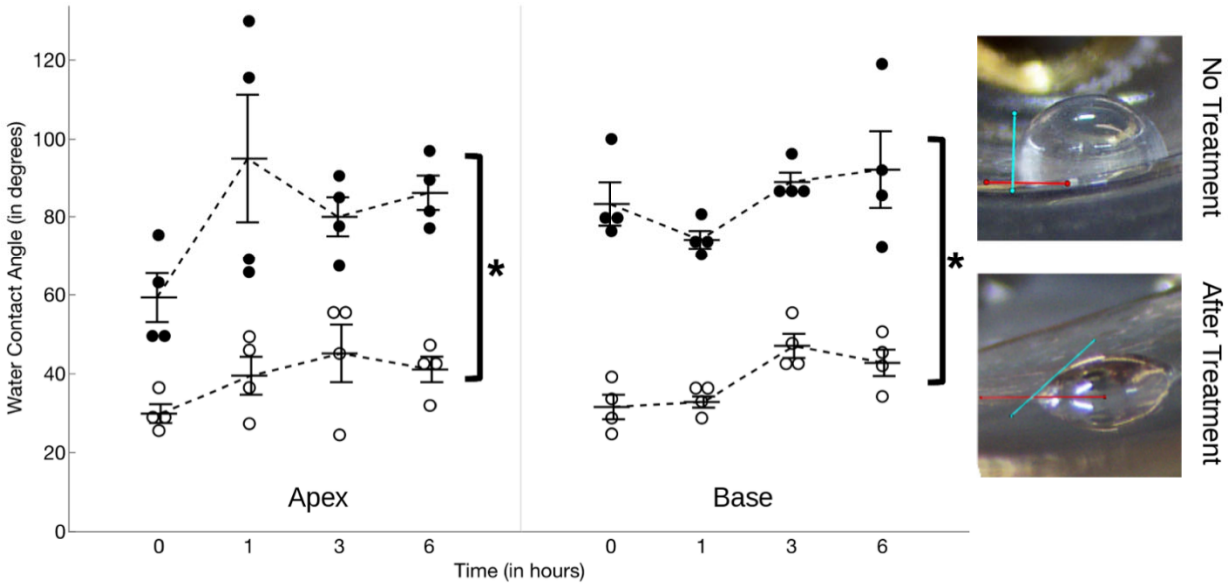

Extended Data Figure 2 | Engineered crystal ribcage surface retains hydrophilicity over entire surface for up to 6 hours. Hydrophilicity measured by the water contact angle of a droplet on a treated vs non-treated crystal ribcage surface. Smaller water contact angles are indicative of a hydrophilic surface.

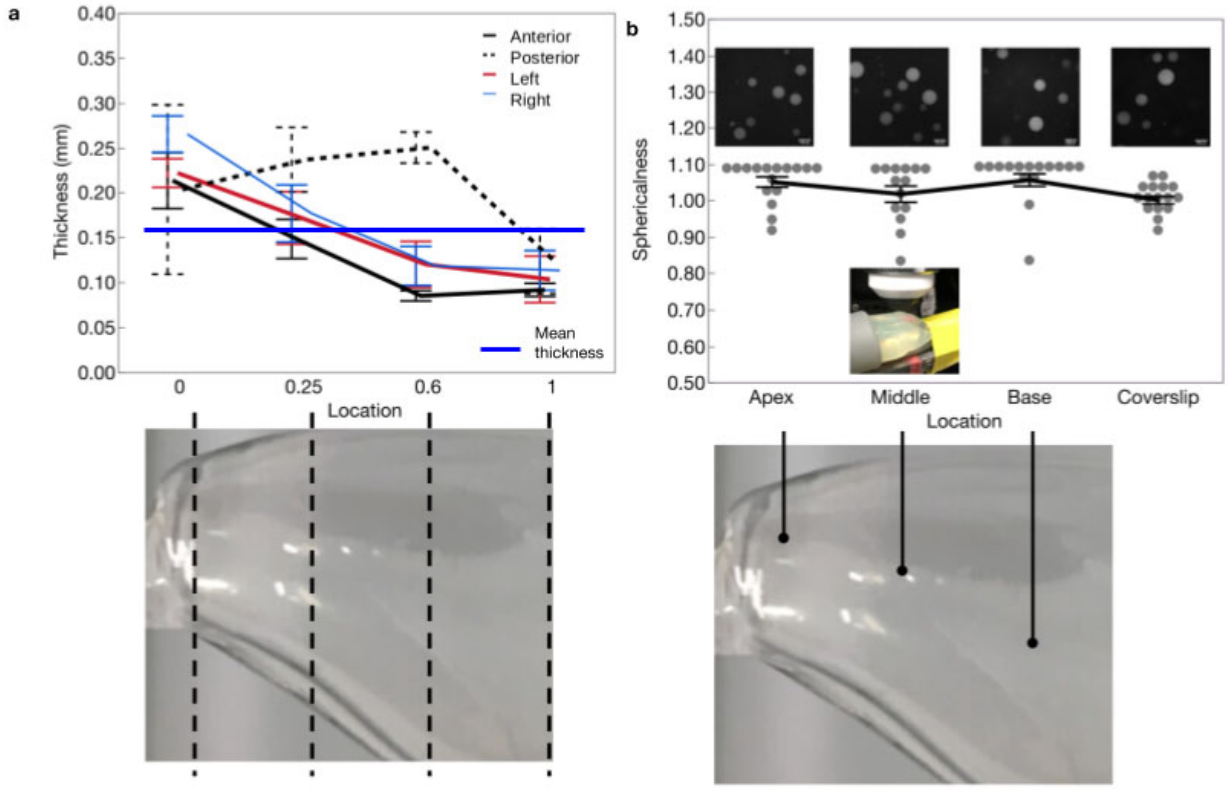

Extended Data Figure 3 | Crystal ribcage has little variation in thickness across its geometry (a) and presents no significant optical aberration over the surface when compared against a coverslip (b). Green-fluorescent polyacrylamide beads with diameters ranging from 40-100 µm were mixed with agarose to make a slurry and uniformly spread over the surface. The beads were imaged using 2-photon microscopy.

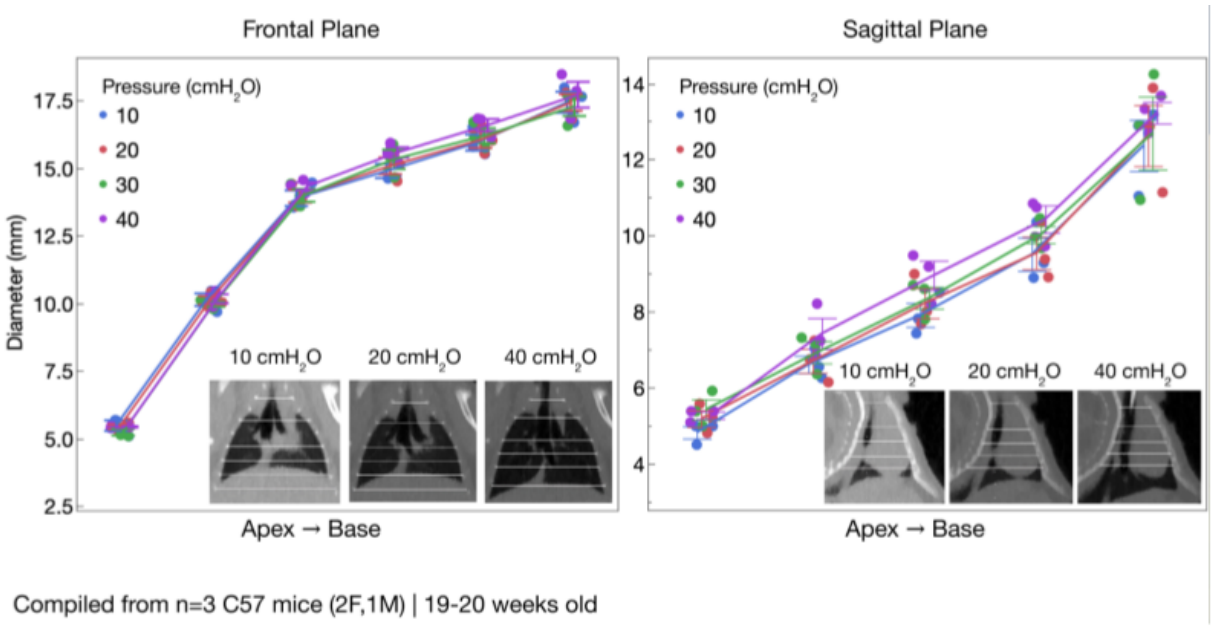

Extended Data Figure 4 | Native mouse ribcage does not show significant variation in diameter with changing PEEP across its anatomy. Previous µCT data used to define the mouse chest cavity was also used to quantify the expansion of the native mouse ribcage as a function of pressure and anatomical location during in situ ventilation. There was no significant difference between the ribcage diameter at tracheal pressures ranging from 10 cmH_2O to 40 cmH_2O in both the frontal and sagittal planes from the apex to the base of the ribcage. The increase in volume with increasing pressure was accommodated by the increasing length of the lung and not the width of the ribcage. This confirms that there was little contribution of the changing ribcage diameter to lung volume change during normal physiological conditions *in situ*.

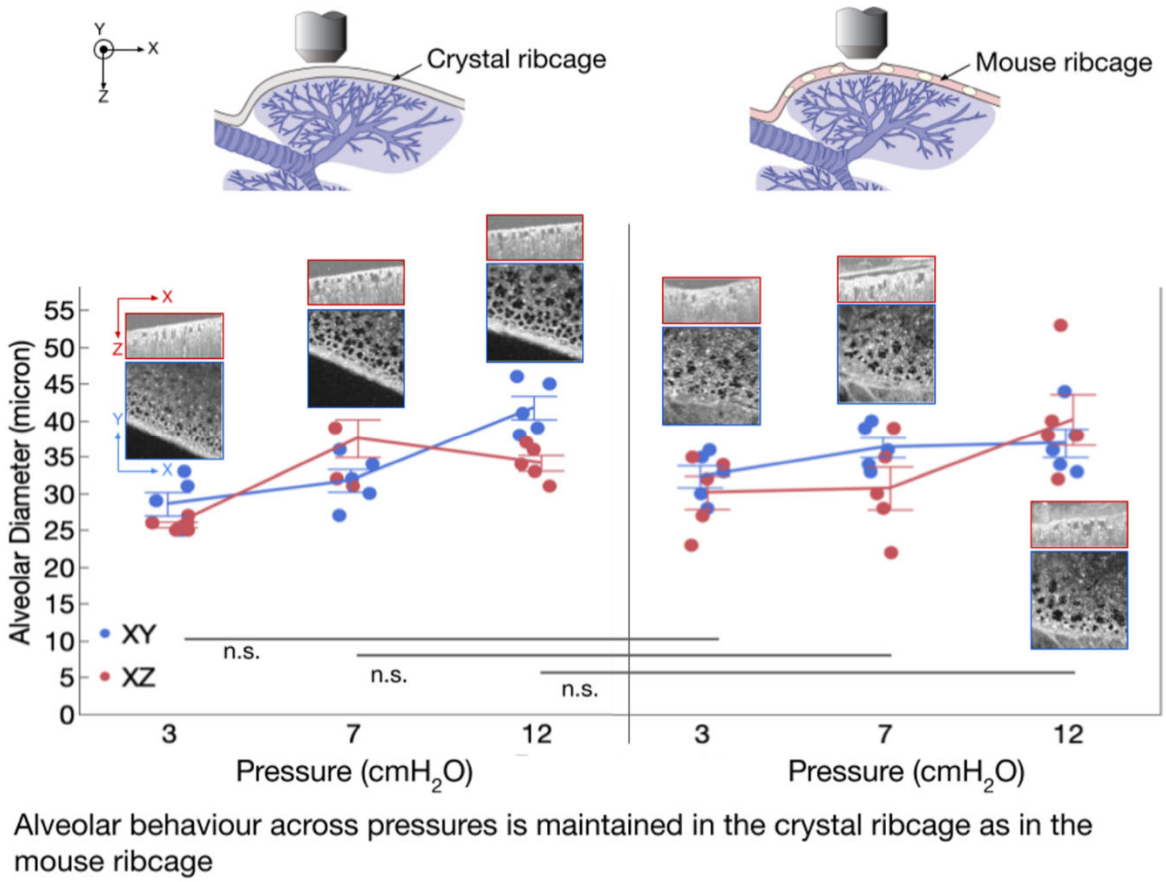

Extended Data Figure 5 | Alveolar function (diameter (µm)) remains unchanged between crystal ribcage and mouse ribcage. A mouse ribcage was thinned down to make a window above the pleural sheath to image the functional lung using OCT, the same lung was then measured in the crystal ribcage for the same changes in pressure. There was no significant difference between alveoli function (measured as changing diameter) across the pressure range.

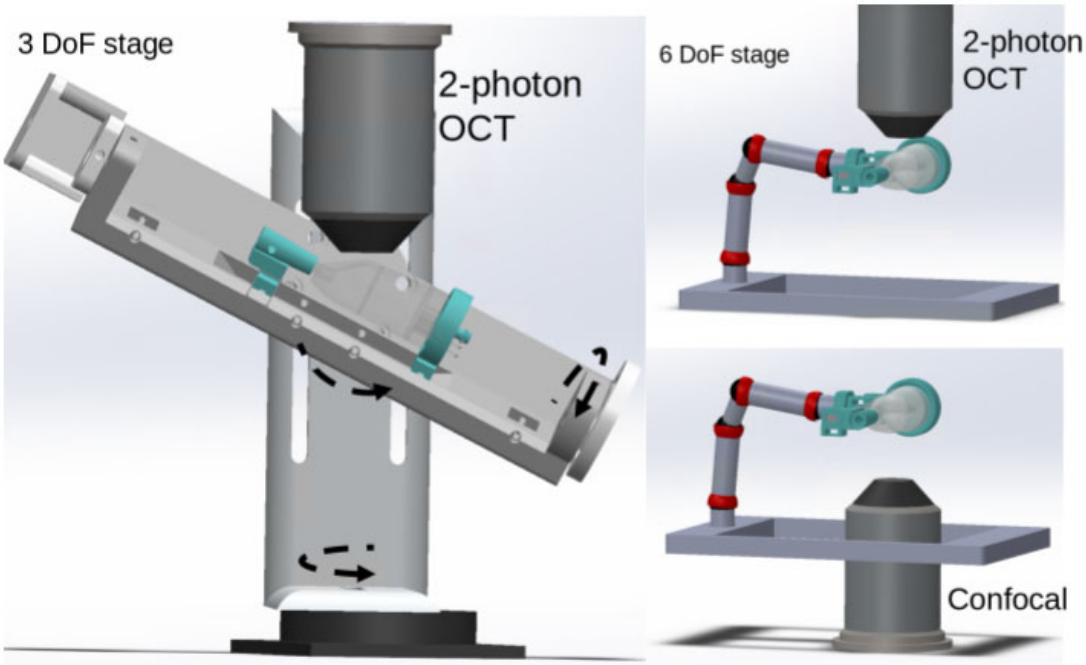

Extended Data Figure 6 | 3D renders of the different degrees of freedom for the arms used to support the crystal ribcage with upright and inverted microscope configurations. We successfully used both stages to image with upright microscopes like the ThorLabs optical coherence tomography probe and Bruker multi-photon microscope. We also successfully used the 6 DoF stage to image lungs with an inverted Olypmus Fluoview 300 laser scanning confocal microscope in addition to the previously mentioned upright microscopes.

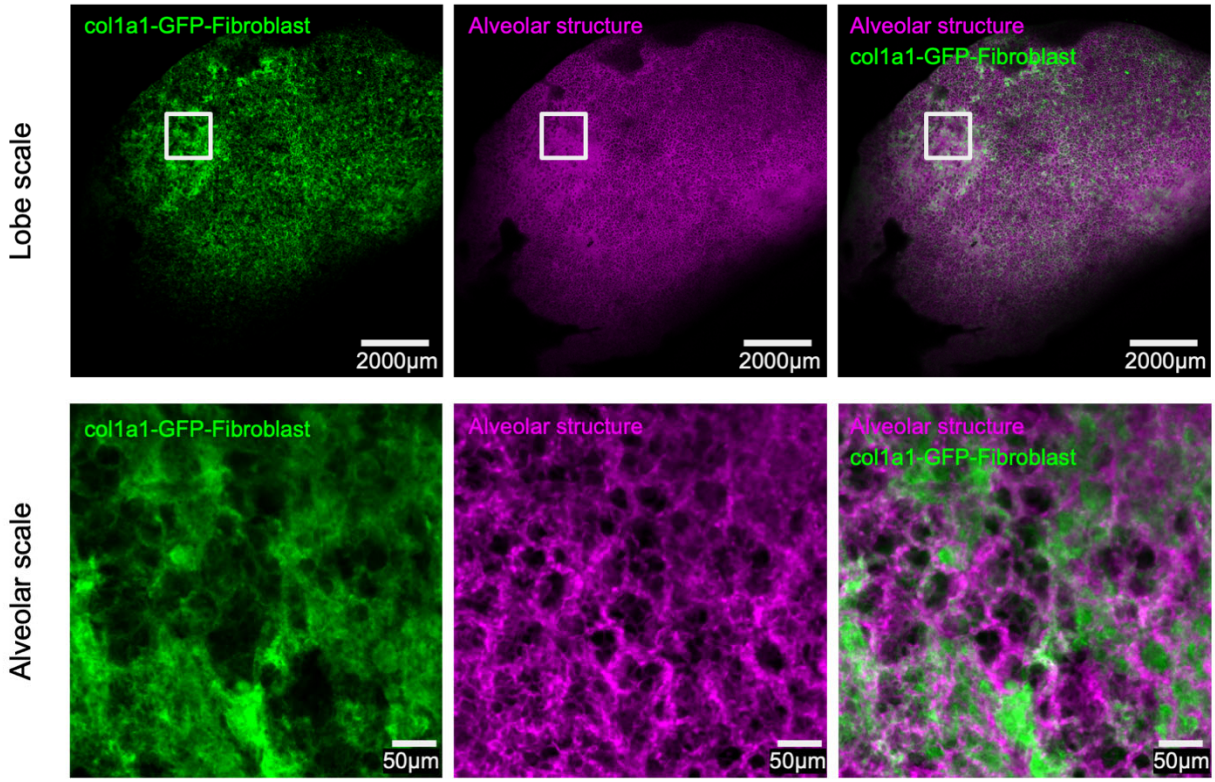

Extended Data Figure 7 | GFP fibroblasts colocalize with tdTomato lesions observed at lobe scale and then again on alveolar structure in tamoxifen treated col1a1-GFP. We subsequently used the regional density in alveolar structure (membrane tdTomato) as a marker for fibrosis in mice that did not have the col1a1-GFP gene.

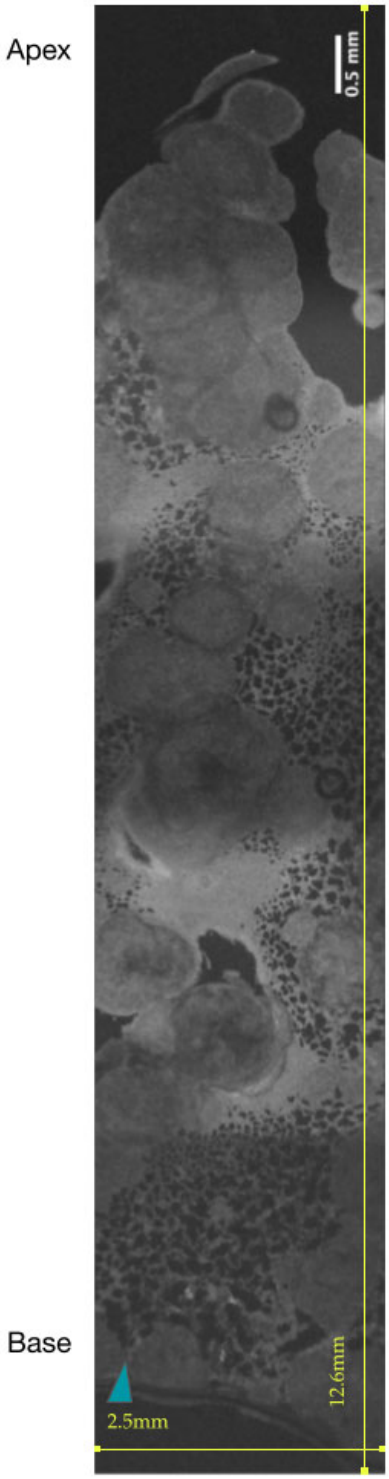

Extended Data Figure 8 | A late-stage nodular tumor afflicted lung through the crystal ribcage from the apex to base at alveolar resolution. The total volume was stitched together from 5 sections using an OCT probe.

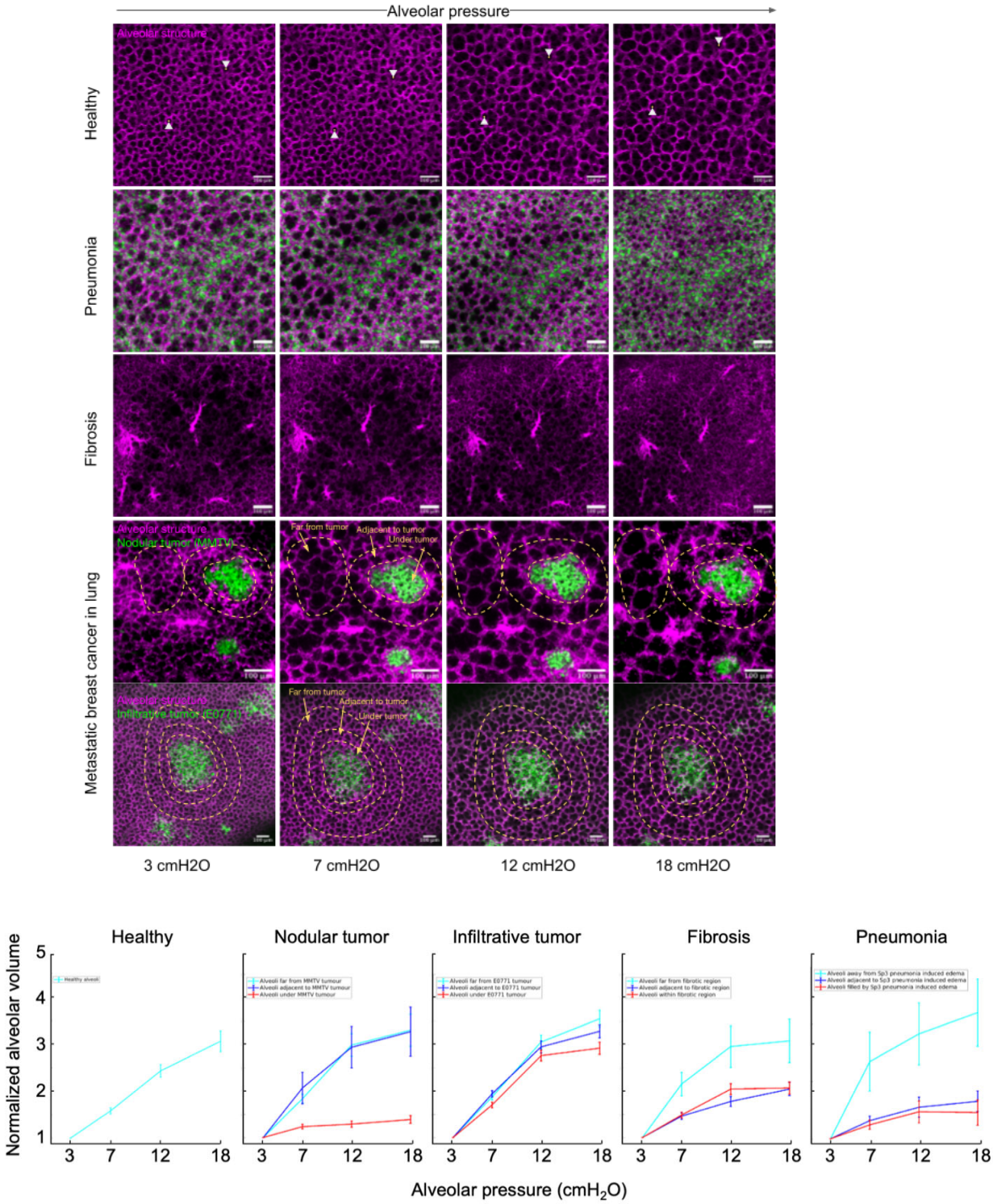

Extended Data Figure 9 | Tracking alveoli along different pressure values through the crystal ribcage. Representative images for different disease conditions**.** Along with the normalized alveolar pressure-volume estimated from the alveolar diameter. N>15 alveoli quantified for each disease condition and group at each alveolar pressure and data presented as mean ± S.E.M.

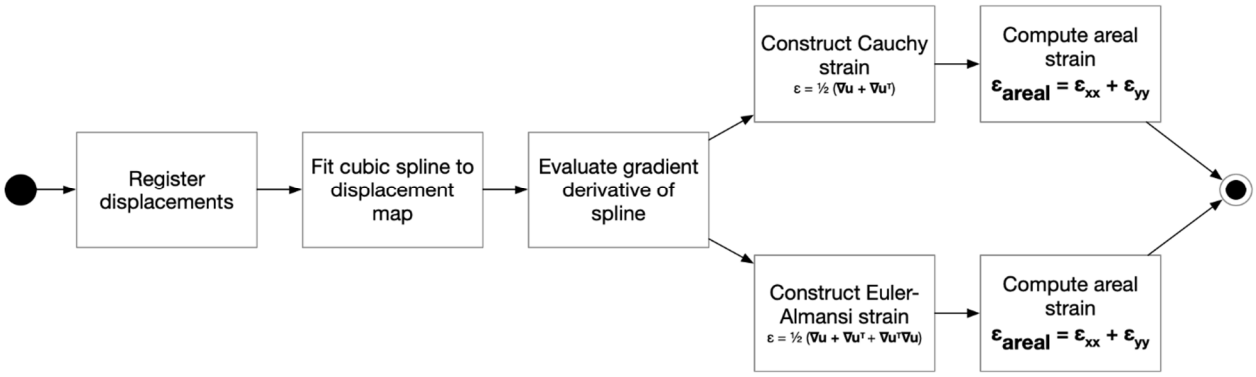

Extended Data Figure 10 | Strain computation workflow.

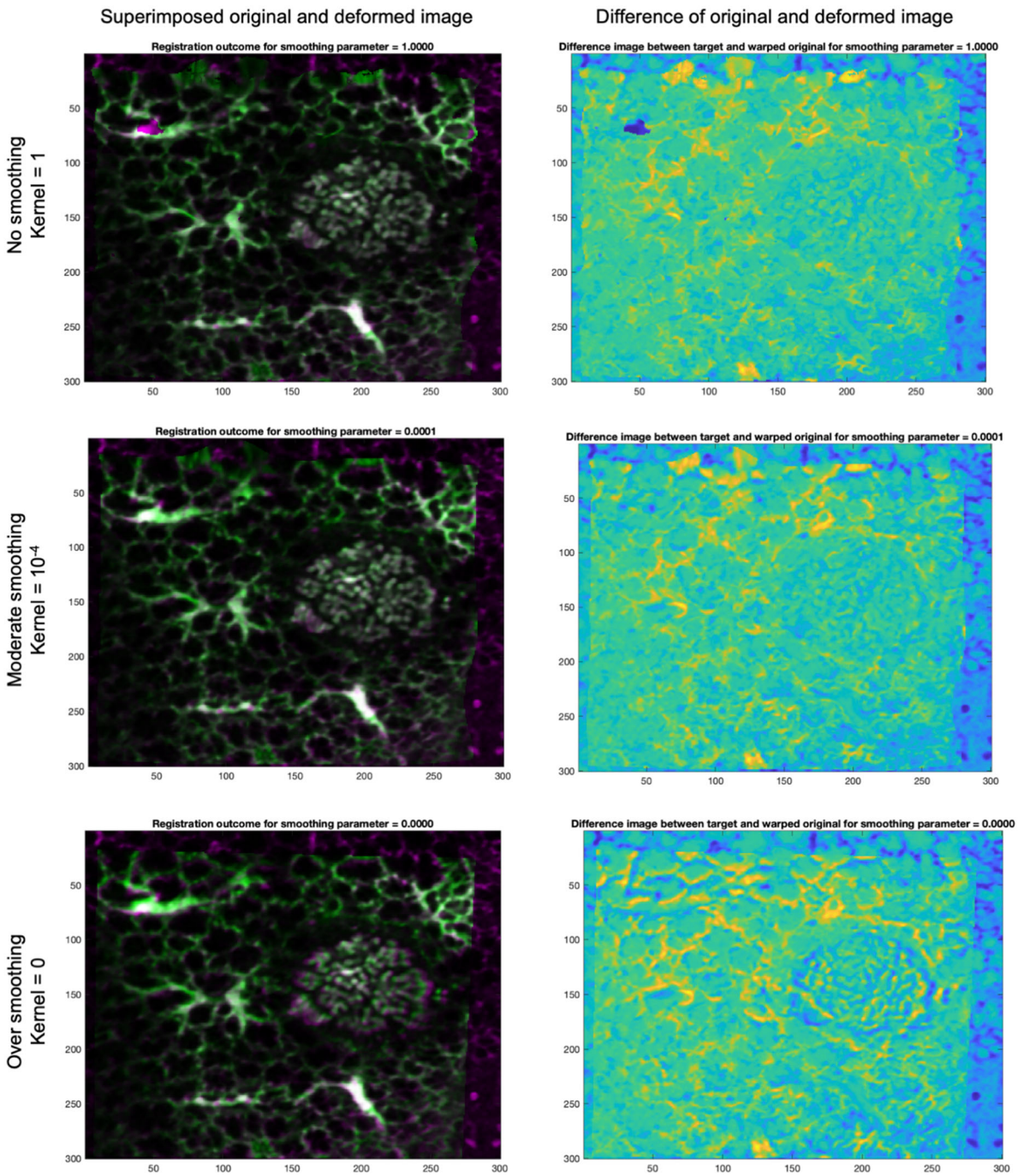

Extended Data Figure 11 | Validation of the effects of smoothing spline on registration quality. The choice of smoothing parameter is important because in the case of over-smoothing where the kernel is 0, the difference image looks significantly different from the control / no smoothing condition with kernel = 1. Comparison of kernels presented 10^{-4} to be a moderate smoothing kernel to preserve the registration integrity.

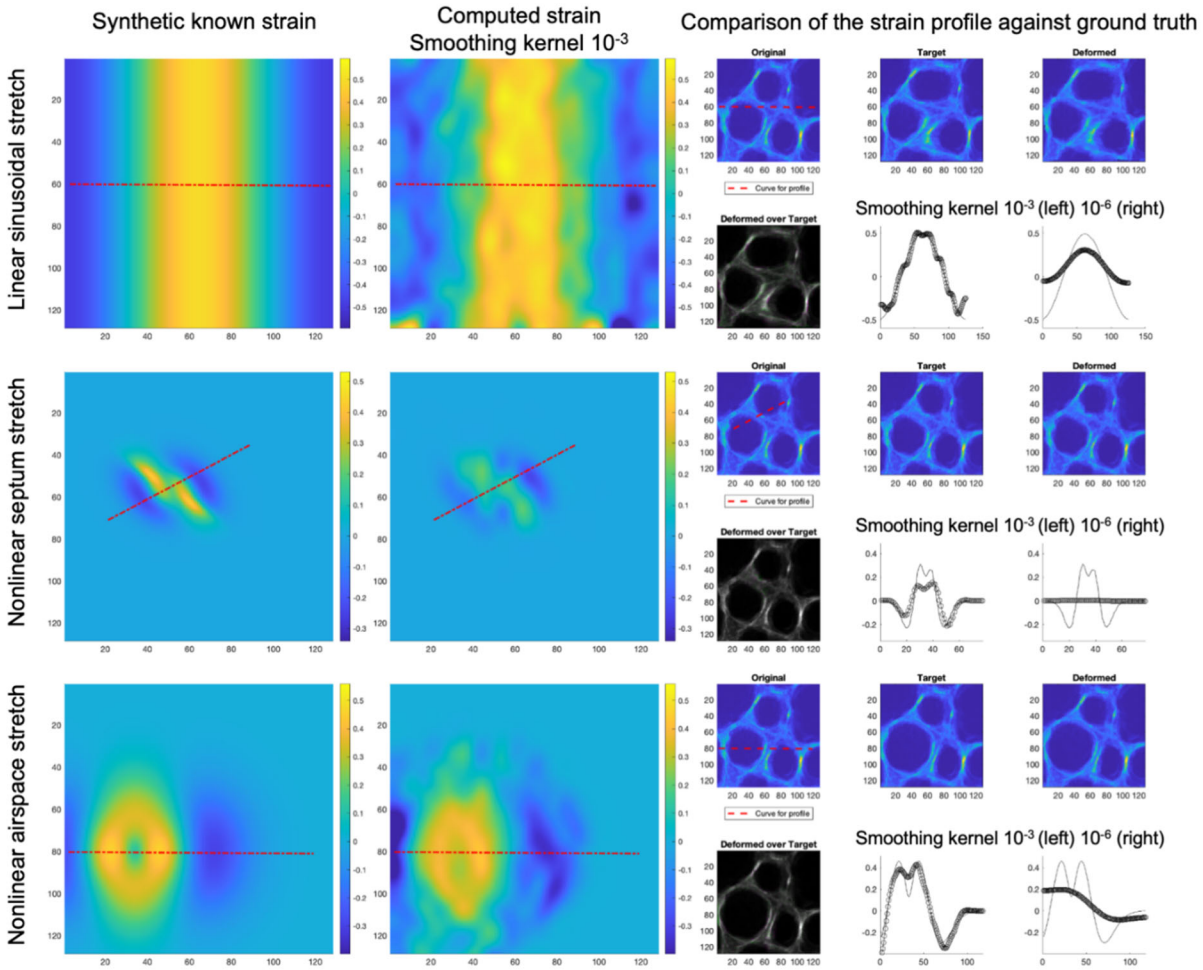

Extended Data Figure 12 | Validation of strain computation for known deformation fields. Computed strain was validated against known strain fields and shows high correspondence when smoothed with a moderate kernel, here 10^{-3}, as compared to a smaller kernel of 10^{-6} which does not capture the applied field.

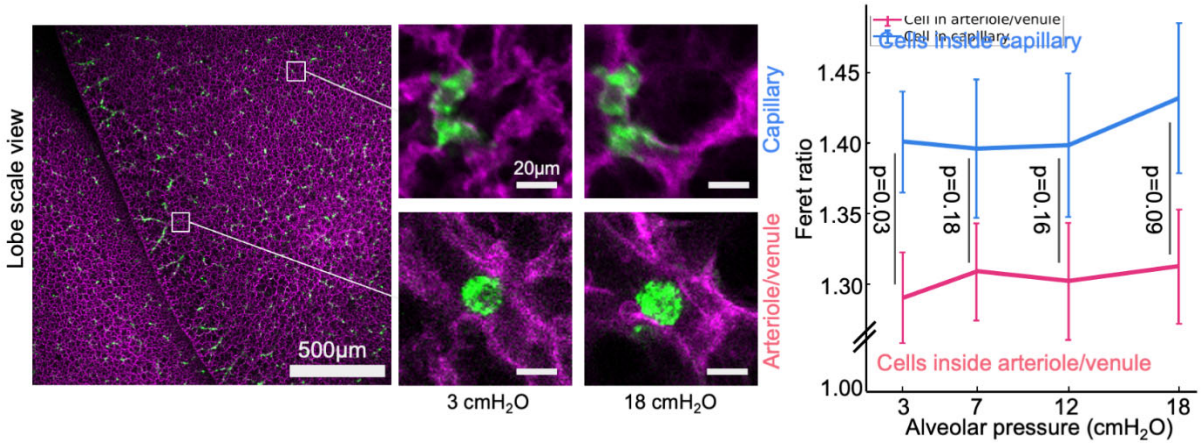

Extended Data Figure 13 | Single cell deformation in response to changing alveolar pressure. Cell-scale imaging with the crystal ribcage showed cancer cells stuck in capillaries trend towards greater deformation (measured by the Feret ratio) compared to cells in larger arterioles-venules. N=40 cells quantified for change in Feret ratio at each alveolar pressure and data presented as mean ± S.E.M.

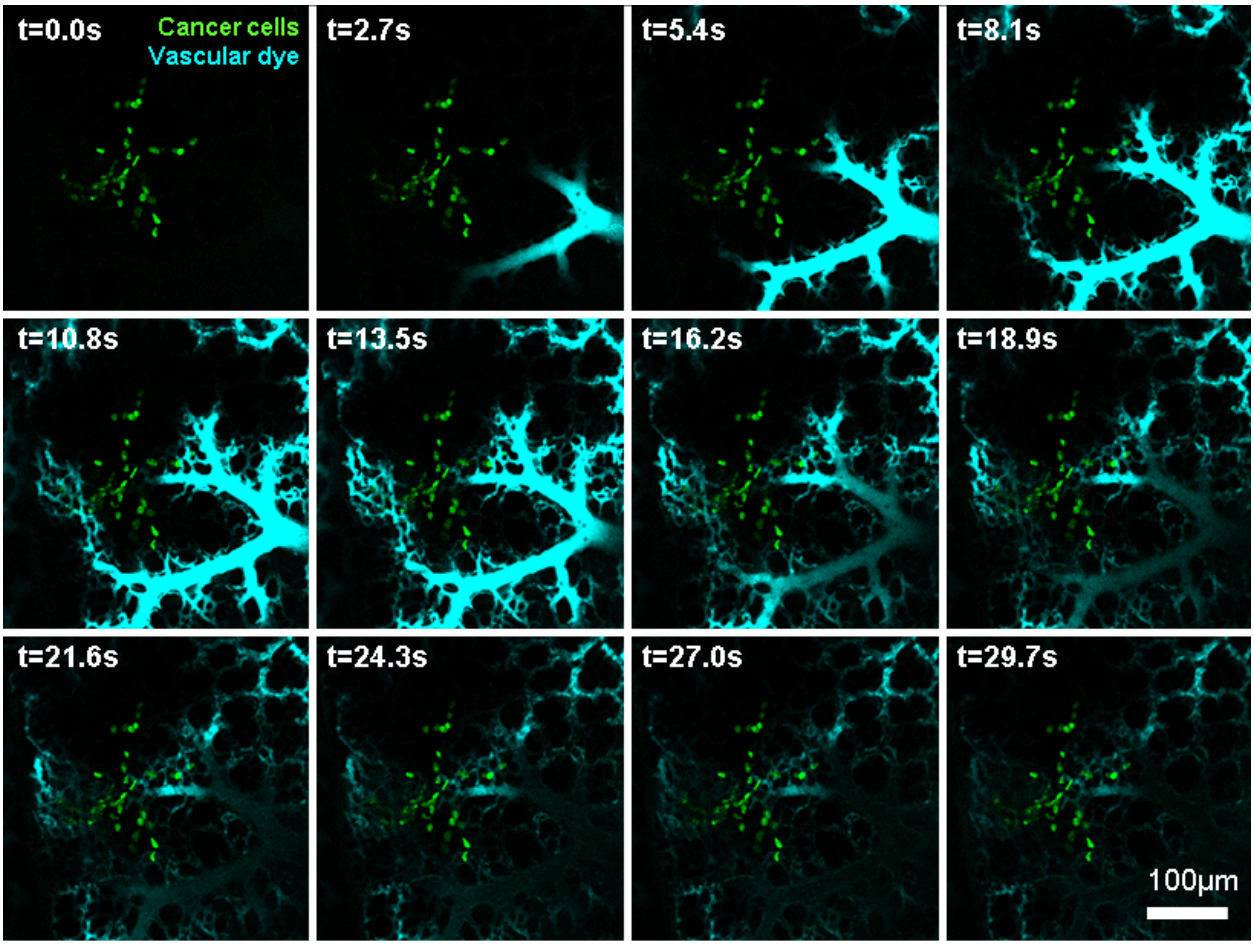

Extended Data Figure 14 | Metastatic cancer cells disrupt vascular dye distribution in capillaries. Capillary scale imaging of single cancer cells that disrupt the distribution of dye observed over a time lapse imaging.

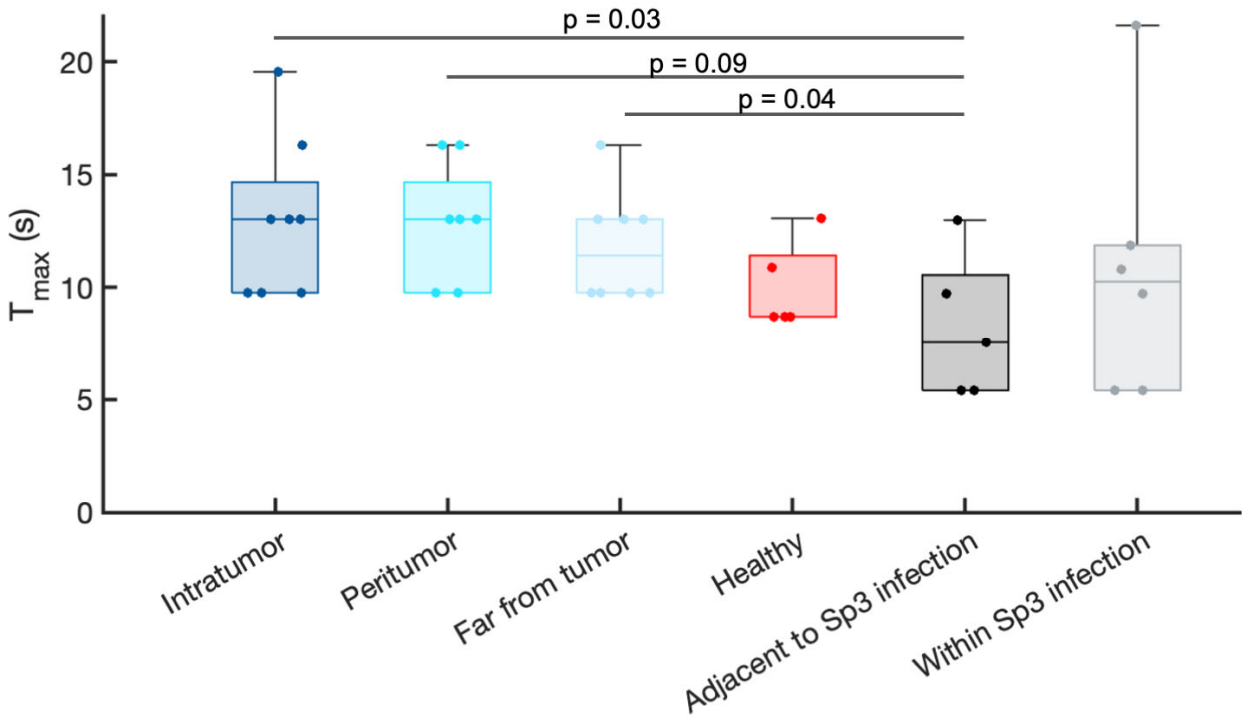

Extended Data Figure 15 | Capillary function is slowest in nodular tumor and fastest in pneumonia conditions. Time taken for dye to reach maximum intensity T_{max} is least in case of pneumonia (Sp3) infection where capillaries are leaky compared to nodular tumor cases.

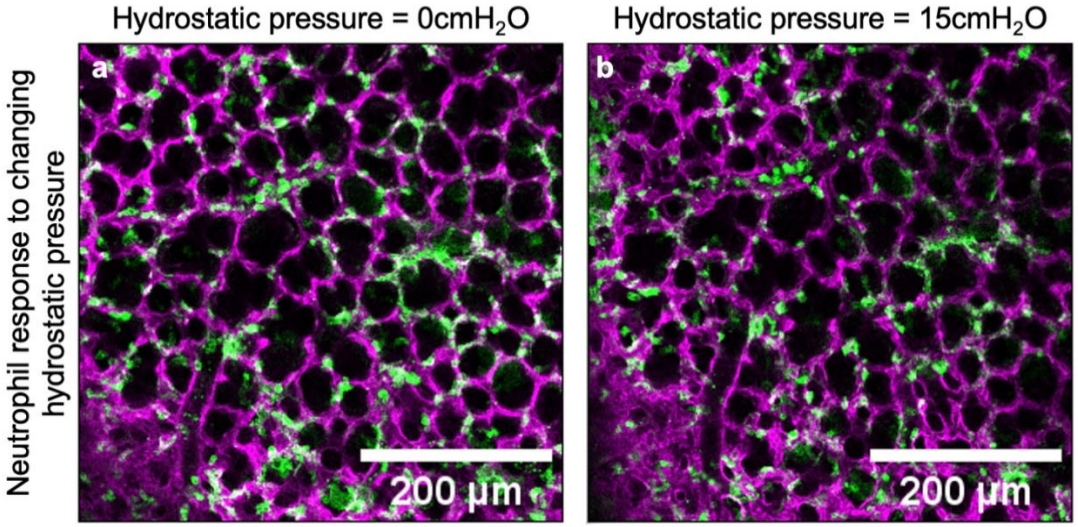

Extended Data Figure 16 | Heterogenous distribution of neutrophils (green) in an alveolar scale image of LPS injured lungs.

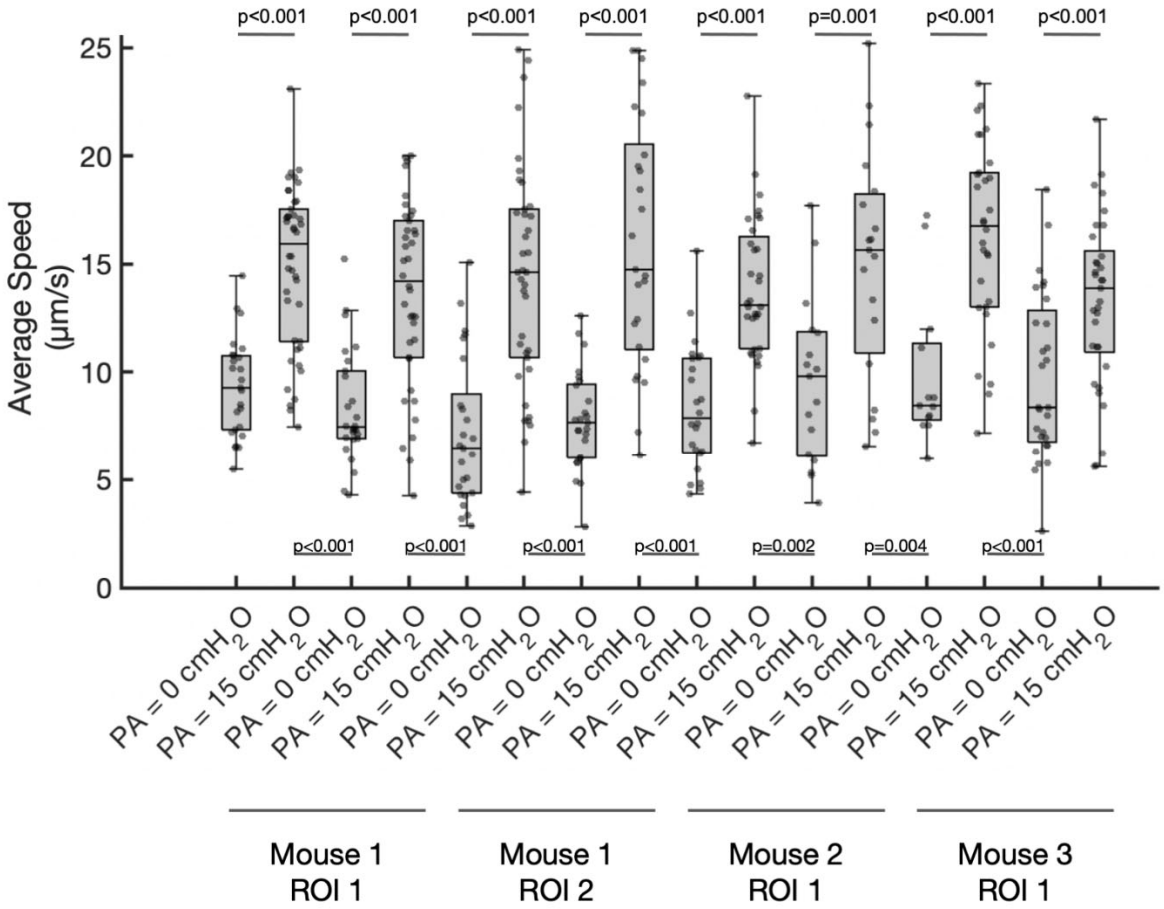

Extended Data Figure 17 | Neutrophil mechano-responsiveness demonstrated in four regions of interest. Hydrostatic pressure inside the capillaries (P_A) reversibly changed from 0 to 15 cmH_2O in n=3 mice and m=4 region of interests.

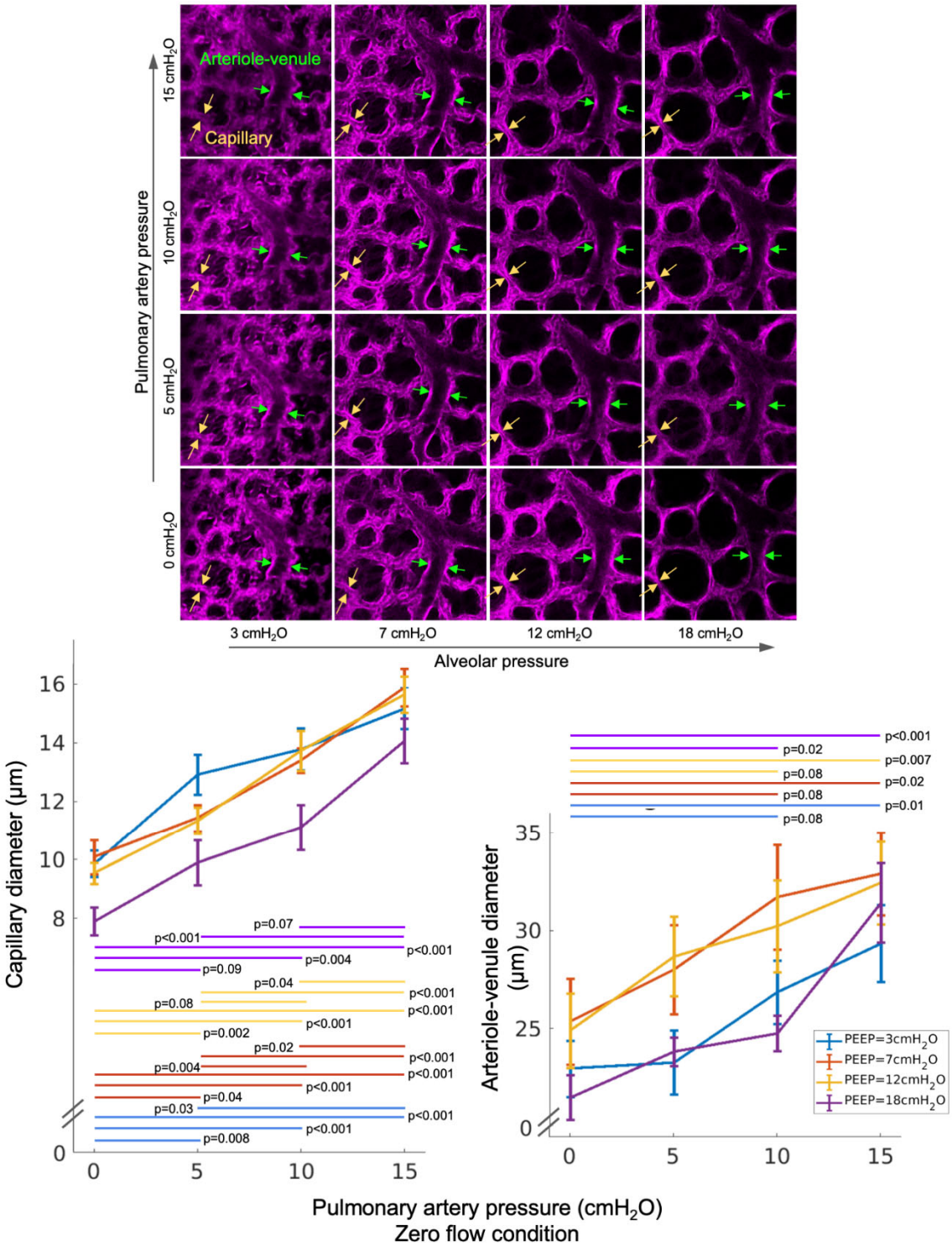

Extended Data Figure 18 | Vessel distension vs vascular pressure. Representative images of arteriole-venules and capillaries imaged over the entire lung surface at different combinations of alveolar and vascular pressures. The changes in vessel diameter (reporting mean ± S.E.M.) with respect to pulmonary artery pressure in zero flow conditions. The vessel diameter significantly increased with increasing pressure for both micro- and medium sized vessels. However, arterioles and venules did not show a significant change in diameter when the pressure was initially increased from 0 to 5cmH$_2$O across all PEEP conditions.

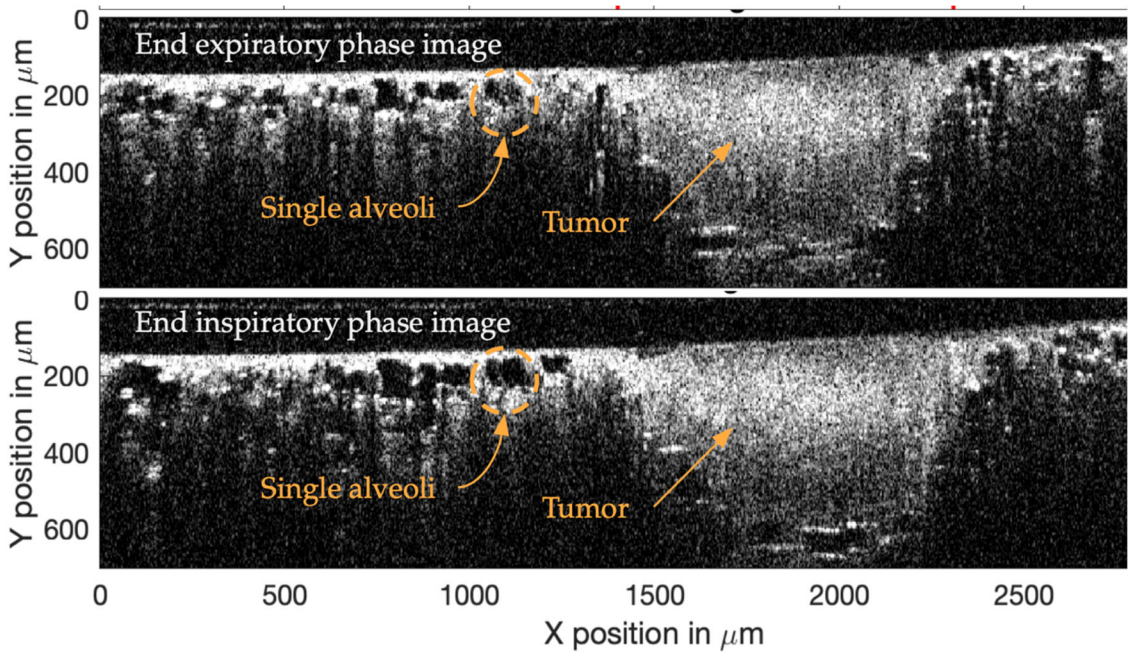

Extended Data Figure 19 | Solid phase nodular growth tumor increases imaging depth in sagittal image section using optical coherence tomography. Alveolar function deeper than 100µm from the surface can be imaged through the tumor nodule up to a depth of 400µm from the surface, as the gas phase of the alveoli is replaced by the solid phase tumor cells which reduces light scattering at the air-liquid interface in the alveoli.